Downslope sediment transport by boiling liquid water under Mars-like conditions: experiments and potential implications for Martian gullies

CLÉMENCE HERNY[1]*, SUSAN J. CONWAY[2], JAN RAACK[3], SABRINA CARPY[2], TANGUY COLLEU-BANSE[2] & MANISH R. PATEL[3,4]

[1]*Physikalisches Institut, Universität Bern, Sidlerstrasse 5, 3012 Bern, Switzerland*

[2]*Laboratoire de Planétologie et Géodynamique – UMR CNRS 6112, Université de Nantes, 2 rue de la Houssinière – BP 92208, 44322 Nantes Cedex 3, France*

[3]*School of Physical Sciences, Faculty of Science, Technology, Engineering & Mathematics, The Open University, Walton Hall, Milton Keynes MK7 6AA, UK*

[4]*Space Science and Technology Department, STFC Rutherford Appleton Laboratory, Harwell Campus, Didcot OX11 0QX, Oxfordshire, UK*

*Correspondence: clemence.herny@space.unibe.ch

Abstract: Gullies are widespread morphological features on Mars for which current changes have been observed. Liquid water has been one of the potential mechanisms to explain their formation and activity. However, under present-day Martian conditions, liquid water is unstable and should only be transiently present in small amounts at the surface. Yet little attention has been paid to the mechanisms by which unstable water transports sediment under low atmospheric pressure. Here we present the results of laboratory experiments studying the interaction between liquid water flowing over a sand bed under Mars-like atmospheric pressure (*c.* 9 mbar). The experiments were performed in a Mars Simulation Chamber (at the Open University, UK), in which we placed a test bed of fine sand at a 25° slope. We chose to investigate the influence of two parameters: the temperature of the water and the temperature of the sand. We performed 27 experiments with nine different combinations of water and sand temperatures ranging from 278 to 297 K. Under all experimental conditions, the water was boiling. We investigated and compared the types and timing of sediment transport events, and the shapes, characteristics and volumes of the resulting morphologies. In agreement with previous laboratory studies we found that more intense boiling increased the volume of sediment transported for a given volume of water. We found four main types of sediment transport: entrainment by overland flow; grain ejection; grain avalanches; and levitation of saturated sand pellets. Our results showed that increasing sand temperature was the main driving parameter in increasing the sand transport and in modifying the dominant sediment transport mechanism. The temperature of the water played a negligible or minor role, apart from the duration of sand ejection and avalanches, which lasted longer at low water temperature. At low sand temperature the majority of the sand was transported by overland flow of the liquid water. At higher sand temperatures the transport was dominated by processes triggered by the boiling behaviour of the water. At the highest temperatures, sediment transport was dominated by the formation of levitating pellets, dry avalanches and ejection of the sand grains. This resulted in a transport volume about nine times greater at a sand temperature of 297 K compared with 278 K. Our heat transfer scaling shows that the boiling behaviour will be enhanced under Martian low gravity, resulting in more efficient transport of sediment by levitating sand pellets even at temperatures close to the triple point. Our results showed that the boiling intensity played an important role in the physics of sediment transport by liquid water. This implied that the amount of water required to produce morphological changes at the surface of Mars could be lower than previously estimated by assuming stable liquid water. Boiling is a critical process to be considered when assessing gully formation and modification mechanisms mobilized by liquid water. Our work could have similar implications for any water-formed landform on Mars, which could include recurring slope lineae, dark dune flows and slope streaks.

Supplementary material: Videos of the experiments are available at https://doi.org/10.6084/m9.figshare.c.3990330

Active flow processes are currently ongoing at the surface of Mars and have been revealed through monitoring campaigns using high-resolution images of landforms such as gullies (Fig. 1; e.g. Malin & Edgett 2000; Costard *et al.* 2002; Mangold *et al.* 2003; Reiss & Jaumann 2003; Védie *et al.* 2008; Diniega *et al.* 2010, 2013; Dundas *et al.* 2010, 2012, 2015; Reiss *et al.* 2010; Jouannic *et al.* 2015; this volume, in review; Raack *et al.* 2015; Pasquon *et al.* 2016; this volume, in review). The physical processes involved in the formation of gullies and their present-day activity have not been unambiguously identified and are

still under debate. Among the proposed mechanisms (see the section 'Gullies on Mars'), liquid water is a strong candidate fluid.

Gullies closely resemble those formed by liquid water on Earth (e.g. Hartmann *et al.* 2003; Marchant & Head 2007), hence the equivalent features on Mars are often considered as an indicator of recent or current liquid water on the surface (e.g. Malin & Edgett 2000; Heldmann & Mellon 2004; Conway & Balme 2016). Although the morphology of these landforms is consistent with their terrestrial counterparts there remain numerous problems for the water hypothesis
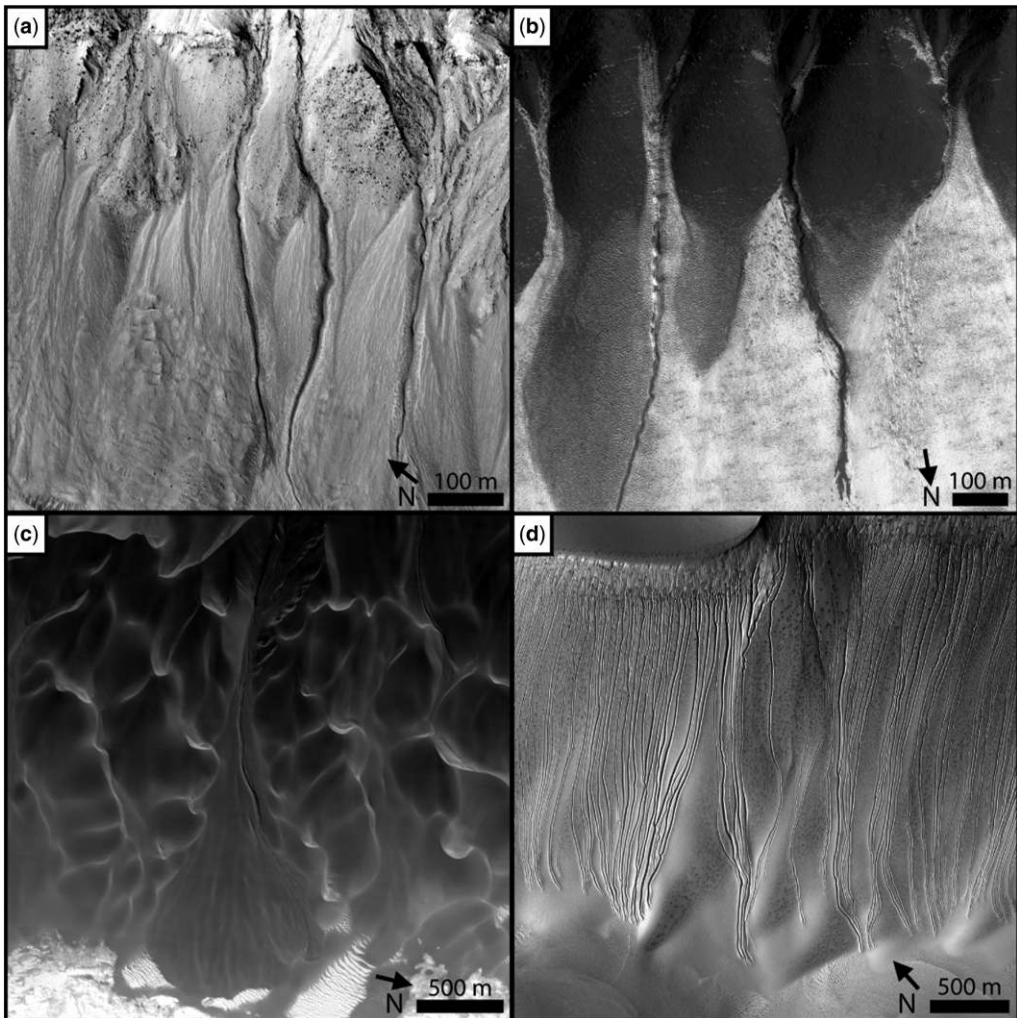

Fig. 1. Examples of mass wasting features for which current activity has been observed. (**a**) New classical gully incision (HiRISE ESP_014093_1410). (**b**) New deposition and dark flows within a classical gully (HiRISE ESP_012332_1115). (**c**) Formation/modification of dune gullies (HiRISE ESP_013478_1300). (**d**) Formation and growth of linear dune gullies (HiRISE PSP_007018_1255).

driving recent activity: (1) liquid water is unstable and can only be produced in limited amounts (e.g. Ingersoll 1970; Haberle *et al.* 2001; Hecht 2002; Richardson & Mischna 2005; Sears & Moore 2005); (2) ongoing activity is recorded at locations and at times of year when the temperature is below the melting point of water (e.g. Diniega *et al.* 2010; Dundas *et al.* 2012; Raack *et al.* 2015; Pasquon *et al.* this volume, in review); (3) volumetrically limited water sources (atmospheric humidity and/or perched topographic aquifers) cannot explain the large numbers of observed features (e.g. Balme *et al.* 2006; Kneissl *et al.* 2010; Harrison *et al.* 2015) or the physical extent of the landforms observed (e.g. Dundas *et al.* 2010, 2015).

Therefore water-based theories have difficulties explaining the source and amount of water required to create and/or modify these metre- to kilometre-scale geomorphological features. Estimations of the volumes of water required to produce the observed changes on Mars are often based on a terrestrial understanding of the behaviour and transport capacity of stable water (Heldmann *et al.* 2005; Pelletier *et al.* 2008; Kolb *et al.* 2010; Parsons & Nimmo 2010). However, recently, Martian-like pressure experiments have highlighted the unusual behaviour of boiling water in sediment transport physics (Massé *et al.* 2016; Raack *et al.* 2017). Boiling of liquid water is thought to occur on Mars as the surface temperatures can locally and temporarily exceed the saturation temperature for the atmospheric pressure (Haberle *et al.* 2001; Reiss & Jaumann 2003; Fenton 2006; Martín-Torres *et al.* 2015). Despite the fact that boiling is likely under present-day conditions, this process has been overlooked to date when liquid water has been proposed as an agent of present-day surface changes. Neglecting the effects of boiling could lead to a bias estimation of the required amount of water involved in mass wasting features and some current activities.

The aim of the paper is to investigate the transport capacity of sediment by liquid water under Martian-like surface conditions. This subject has received only limited experimental investigation so far (see the section 'Previous experimental investigations'), although it can potentially be of primary importance for the understanding and interpretation of water-driven processes and present-day surface activity on Mars. Hence, we conducted a series of experiments under low pressure to study the influence of boiling intensity on sediment transport. The experimental observations are then compared with physical laws in order to understand the important parameters driving the sediment transport by unstable water. Finally, we performed scaling to Martian gravity, in order to apply our results to Martian features.

State of art

Stability of liquid water at the surface of Mars

Climate models, experimental investigations and remote sensing data have shown that only transient and restricted amounts of water can flow on present-day Mars because it is highly unstable owing to low pressure and a dry atmosphere (e.g. Ingersoll 1970; Kieffer *et al.* 1977; Haberle *et al.* 2001; Lobitz *et al.* 2001; Smith *et al.* 2001; Hecht 2002; Richardson & Wilson 2002; Kossacki & Markiewicz 2004; Richardson & Mischna 2005; Sears & Moore 2005; Chevrier *et al.* 2009; Reiss *et al.* 2010; McEwen *et al.* 2011, 2014; Grimm *et al.* 2014; Ojha *et al.* 2015; Stillman *et al.* 2016; Martín-Torres *et al.* 2015). The range of temperatures over which liquid water is stable is narrow, from about 274 to 281 K (Wagner *et al.* 2011) for an atmospheric pressure range between 6.5 and 10 mbar on Mars (Hess *et al.* 1980; Hourdin *et al.* 1995; Haberle *et al.* 2001). Therefore, if the surface temperature reaches or exceeds the melting temperature ($T_0 > 273$ K at $P > 610$ Pa, above the triple point) then water potentially boils shortly afterwards. Surface temperatures on Mars can locally exceed 285 K (Haberle *et al.* 2001; Reiss & Jaumann 2003; Fenton 2006; McEwen *et al.* 2014; Martín-Torres *et al.* 2015) and therefore potentially exceed both the melting and boiling points. Boiling is a complex process that increases the rate of phase change compared with evaporation and results in a decreased lifetime of liquid water. Vapour bubbles start to nucleate at the solid–liquid interface according to the surface tension. Formation of gas bubbles is favoured when the surface tension increases as the atmospheric pressure and temperature of the liquid–gas interface decrease (Cengel & Ghajar 2014; Giraud *et al.* 2015). Surface roughness also favours bubble formation, because it creates nucleation sites required for bubble initiation. Any water flowing on Mars would encounter rough sediments and rocks, which would encourage boiling.

The range of conditions allowing liquid water can be broadened if dissolved salts (brines) are considered as the presence of salts depressing the melting point and evaporation rate (Brass 1980; Sears & Chittenden 2005; Möhlmann & Kereszturi 2010; Masterton & Hurley 2011; Nuding *et al.* 2015). Although evaporation has been considered in previous studies of water flow at the Martian surface (e.g. Heldmann *et al.* 2005), the physical effects of boiling are usually not taken into account.

Gullies on Mars

Gullies on Mars (Fig. 1) are one of the most common mass wasting features and were first identified by Malin & Edgett (2000). In general they can be

divided into three types: (1) 'classical gullies' (Fig. 1a, b; e.g. Malin & Edgett 2000; 2006; Balme *et al.* 2006; Dickson *et al.* 2007; Dundas *et al.* 2010, 2012, 2015, 2018; Harrison *et al.* 2015; Raack *et al.* 2015; Conway *et al.* 2015, 2018); (2) 'dune gullies' (Fig. 1c; e.g. Diniega *et al.* 2010; Hansen *et al.* 2011, 2013; Dundas *et al.* 2012, 2015; Harrison *et al.* 2015); and (3) 'linear dune gullies' (Fig. 1d; e.g. Costard *et al.* 2002; Mangold *et al.* 2003; Reiss & Jaumann 2003; Védie *et al.* 2008; Reiss *et al.* 2010; Dundas *et al.* 2012; Diniega *et al.* 2013; Jouannic *et al.* 2015; Pasquon *et al.* 2016).

Several mechanisms have been proposed to explain their formation and current activity: (1) liquid groundwater release (e.g. Malin & Edgett 2000; Gaidos 2001; Mellon & Phillips 2001; Gilmore & Phillips 2002; Heldmann & Mellon 2004; Heldmann *et al.* 2005, 2007; Malin *et al.* 2006); (2) melting of near-surface snow or ice in a warmer recent past (e.g. Costard *et al.* 2002; Arfstrom & Hartmann 2005; Berman *et al.* 2005; Head *et al.* 2008; Védie *et al.* 2008; Schon *et al.* 2009; Williams *et al.* 2009; Kneissl *et al.* 2010; Raack *et al.* 2012; Jouannic *et al.* 2015); (3) melting of surface snow or ice under current climatic conditions (Christensen 2003; Head *et al.* 2008); (4) CO$_2$-supported flows (e.g. Hoffman 2000, 2002; Musselwhite *et al.* 2001; Stewart & Nimmo 2002; Ishii & Sasaki 2004; Hugenholtz 2008; Di Achille *et al.* 2008; Dundas *et al.* 2010, 2012; Cedillo-Flores *et al.* 2011; Hansen *et al.* 2011; Diniega *et al.* 2013; Pilorget & Forget 2015; Raack *et al.* 2015); and (5) dry granular flows (e.g. Treiman 2003; Shinbrot *et al.* 2004; Pelletier *et al.* 2008; Kolb *et al.* 2010). So far none of the proposed mechanisms is able to completely explain all their morphological features, their distribution and their present-day activity.

As mentioned in the previous section 'Stability of liquid water at the surface of Mars', surface temperature can currently exceed the melting point and potentially the boiling point at the surface of Mars. These conditions occur mainly on equator-facing slopes situated on the walls and/or dunes fields of Valles Marineris, and in low topographic basins, pits and craters (where the pressure is higher) from 45° N to 70° S. Within these latitudes active linear dune gullies (e.g. Mangold *et al.* 2003; Reiss & Jaumann 2003; Miyamoto *et al.* 2004; Reiss *et al.* 2010; Jouannic *et al.* 2012) and very recent classical gullies (e.g. Reiss *et al.* 2004; Raack *et al.* 2012) can be found, which strengthens the case for an involvement of liquid water. Therefore despite its instability, liquid water flows remain a strong candidate for the formation of gullies in the past and present (e.g. Malin & Edgett 2000; Mangold *et al.* 2003, 2010; Reiss & Jaumann 2003; Miyamoto *et al.* 2004; Heldmann *et al.* 2005; Mushkin *et al.* 2010; Reiss *et al.* 2010; Conway *et al.* 2015; Conway & Balme 2016).

Previous experimental investigations

Only a few experiments have been performed which study the transport of sediments by liquid water under low pressure. In these experiments, landforms were created by liquid water flowing over an inclined sediment surface under Martian pressure rather than under terrestrial pressure (Conway *et al.* 2011; Jouannic *et al.* 2015; Massé *et al.* 2016; Raack *et al.* 2017). These experiments reveal that at low pressures sand temperature plays a crucial role in the development of landforms and the process of sediment transport by unstable water.

Experiments led by Conway *et al.* (2011) at Martian and terrestrial pressures have shown that water flow over frozen dry sediments (*c.* 273 K) has a greater runoff length and erosion rate than at higher temperatures owing to the formation of ice lenses. This inhibits water infiltration, liberating more water to transport sediment and leading to a longer and a faster flow (Conway *et al.* 2011). If the substrate is already wet and frozen, the liquid water does not infiltrate at all (Jouannic *et al.* 2015). In this case the resulting debris flow morphologies formed during experiments under Martian and terrestrial pressures are more comparable. For both of these experiments (Conway *et al.* 2011; Jouannic *et al.* 2015) simultaneous freezing and boiling of the flowing water was observed. Recently, experiments under Martian pressures with a relatively warm substrate ($\geq$288 K) have revealed new transportation mechanisms involving both wet and dry processes (Massé *et al.* 2016; Raack *et al.* 2017). (1) The melting of an ice block at the top of a sand bed between 288 and 293 K and under Martian pressure releases liquid water. Massé *et al.* (2016) described for the first time how boiling water provokes ejection of sand particles while the liquid flow percolates downslope. The combination of these transport mechanisms triggers the formation of arcuate sand ridges perpendicular to the flow direction and dry sand avalanches. For similar configuration, but at terrestrial pressure, only water percolation is observed without sediment transport (Massé *et al.* 2016). (2) Raack *et al.* (2017) described another new flow processes associated with boiling water. The interaction between boiling water and warm sediment ($T_s \approx 297$ K) triggered the formation of wet sand pellets that levitate and travel downslope carving an ephemeral sinuous transportation channel. This unusual transport mechanism occurs in parallel with sand ejection, dry sand avalanches, overland flow and infiltration. These previous experiments (Massé *et al.* 2016; Raack *et al.* 2017) demonstrated that boiling liquid water has a much larger sediment transport capacity than stable liquid water.

All of these experiments have shown that unstable water can have unexpected effects on the

behaviour of a sediment-laden flow, in terms of sediment transport mechanisms, morphologies and dynamics. In particular they demonstrate that under specific environmental conditions (low pressure, warm sediment) less liquid water is needed to transport sediment compared with under 'normal' terrestrial conditions. These results emphasize that the stability of water needs to be taken into account for orbital data interpretation, scaling laws and numerical modelling of active (and potentially past) water-based Martian surface processes.

The experiments presented here also investigate the role of boiling intensity in the formation of mass wasting morphologies produced by liquid water flow over a sediment bed at Martian pressure. Among the many potential controlling parameters (atmospheric pressure, water vapour partial pressure, temperature, gravity), we chose to study two of them: (1) the water temperature; and (2) the sand temperature. These two parameters were chosen respectively because the water temperature plays a role in boiling during phreomagmatic eruptions and geysers (Lorenz 2002) and the sand temperature is thought to drive the boiling intensity at a given pressure (Cengel & Ghajar 2014). The range of temperatures (from 278 to 297 K), for both water and sand, is consistent with a minimum value that allows water boiling at a chosen pressure and a maximum value close to the maximum temperatures measured at the surface of Mars. Experiments previously presented by Raack et al. (2017) showed that, at a constant water temperature, an increase in the sand temperature of less than 20 K strongly intensified the physical processes and increased sediment transport by a factor of c. 9. The influence of water temperature has not yet been investigated. To evaluate the respective importance of the water and sand temperature in the interaction of unstable water with loose sediment we performed a systematic exploration of both these temperature parameters.

Methods

We performed experiments using nine different combinations of water and sand temperatures in triplicate for a total of 27 experiments. The experimental procedure is similar to those presented by Raack et al. (2017), whose experimental results are also included in this work. An overview of the temperature conditions used in the experiments are presented in Table 1.

Experimental set-up and instrumentation

The experiments were performed under Martian-like pressure in a cylindrical low pressure chamber, 2 m in length and 0.9 m in diameter (Fig. 2) at the Open University (Mars Simulation Chamber facility – MSC). The air inside the chamber was evacuated by two vacuums pumps and pressure was recorded every second by a pressure sensor (Pirani gauge). We started each experiment when a pressure of c. 7 mbar was reached. Owing to the production of water vapour inside the chamber as the liquid water was introduced the total pressure increased until it reached a constant value close to an average value. The average pressure for all experiments during the 60 s of water flow were 9.6 mbar, which is within the range of possible pressures on Mars (between 6.5 and 10 mbar; Hess et al. 1980; Hourdin et al. 1995; Haberle et al. 2001).

The test bed was placed in a rectangular metallic tray (0.9 m long, 0.4 m wide and 0.1 m deep), which was then set inside the MSC at an angle of 25° (Figs 2b & 3). This angle was chosen close to the slope values observed in the source areas of classical gullies (Pouliquen 1999; Heldmann & Mellon 2004; Dickson et al. 2007; Pelletier et al. 2008; Parsons & Nimmo 2010; Conway et al. 2015). The chosen 25° slope also falls between the slightly shallower slopes of active polar gullies (dark flows within

Table 1. *Overview of water and sand temperature configurations for the performed experimental runs including run identifiers used in the rest of this paper*

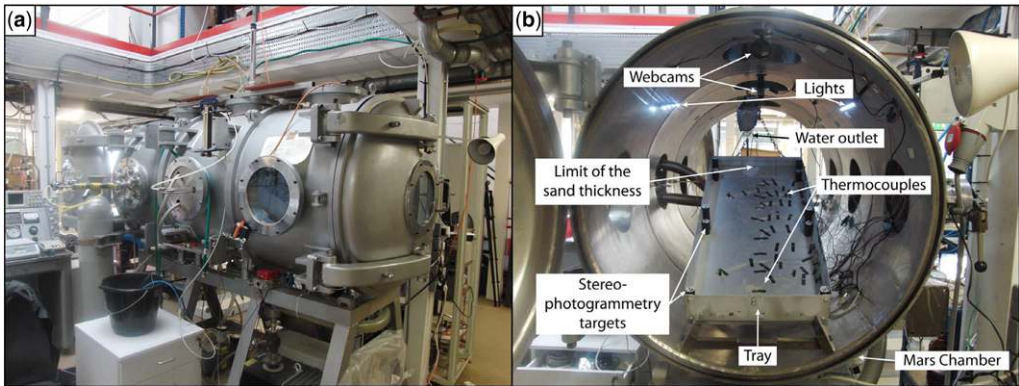|		Sand temperature (K)		
		278	288	297
Water temperature (K)	278	S278-W278-1	S288-W278-1	S297-W278-1
		S278-W278-2	S288-W278-2	S297-W278-2
		S278-W278-3	S288-W278-3	S297-W278-3
	288	S278-W288-1	S288-W288-1	S297-W288-1
		S278-W288-2	S288-W288-2	S297-W288-2
		S278-W288-3	S288-W288-3	S297-W288-3
	297	S278-W297-1	S288-W297-1	S297-W297-1
		S278-W297-2	S288-W297-2	S297-W297-2
		S278-W297-3	S288-W297-3	S297-W297-3

Fig. 2. Mars Simulation Chamber (MSC) at the Open University (Milton Keynes, UK). The chamber is 2 m in length and 0.9 m in diameter. (**a**) Exterior view of the MSC. (**b**) Interior view of the MSC with relevant experimental apparatus labelled. Note: the sand has been removed for this photograph.

existing gullies at *c.* 15°; Raack *et al.* 2015) and of active linear dune gullies (*c.* 10–20°; Reiss *et al.* 2010; Pasquon *et al.* 2016) and the steep slopes around 28–35° of active Recurring Slope Lineae (McEwen *et al.* 2011; Ojha *et al.* 2014; Stillman *et al.* 2014, 2016). Furthermore, this angle is less than the angle of repose of the sand on both Earth and Mars (Kleinhans *et al.* 2011; Atwood-Stone & McEwen 2013), which means that the sediments do not fail with slight vibrations/perturbations. The tray contains black lines at 5 cm from its base and perpendicular lines every 10 cm on the side walls to assist in levelling the sand and to calibrate distances along the tray observed in images/videos.

All of the experiments were performed with a natural aeolian fine silica sand (modal diameter of the grains $D_{50} = 2.3 \times 10^{-4}$ m and minor components of clay and silt), which was also used in previous experiments in the MSC at the Open University (Conway *et al.* 2011; Jouannic *et al.* 2015; Massé *et al.* 2016; Raack *et al.* 2017). This sediment is a reasonable analogue for loose sediments on Mars because its grain size is intermediate between coarser sand grains of most Martian dunes (e.g. coarser than *c.* 210 µm with a mean of larger than *c.* 430 µm; Edgett & Christensen 1991) and finer material observed in the ripple troughs of Bagnold dunes at Gale Crater (e.g. *c.* 150 µm; Bridges *et al.* 2017; Lapotre *et al.*
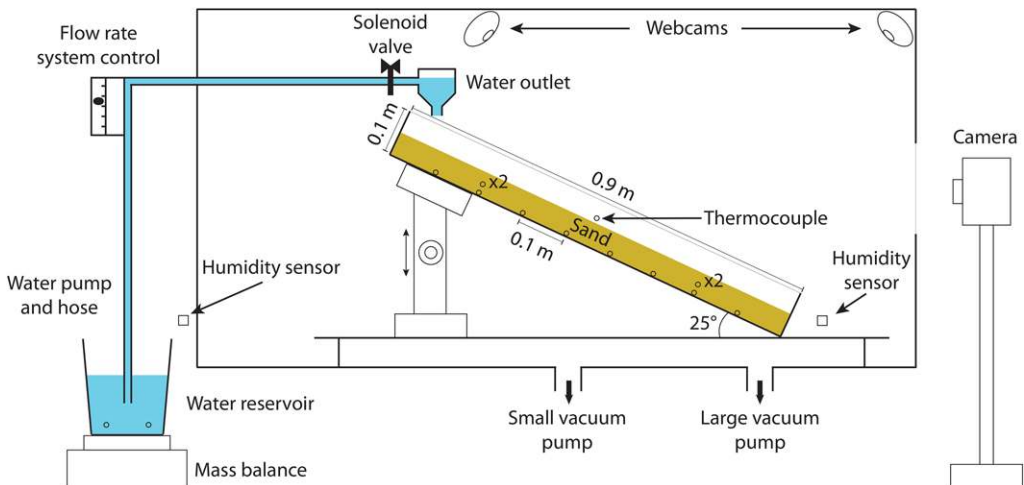

Fig. 3. Diagram of the experimental set-up. The black circles indicate the position of the thermocouples (TC). The '×2' label indicates that there are two thermocouples at different horizontal positions on the tray. These thermocouples are placed at 10 cm from the right and left border of the tray, respectively.

2017; Johnson et al. 2017). We used a sediment bed of c. 5 cm thickness to have a sufficient thickness of sediment so that the base of the tray would not be exposed by the flow and hence would not influence sediment transport. To set the test bed to the desired temperature, the sand was, as necessary, pre-chilled in a freezer.

The water outlet inside the MSC was placed at the top and in the centre of the test bed (c. 8 cm from the upper edge), 1.5 cm above the sediment surface, which was used for practical reasons: this height was the minimum height we could use without disrupting the trajectory of the ejected sediment. A reservoir of liquid water was placed outside of the chamber at a controlled temperature. The water was transported from the reservoir via a hose and a pump which was used to maintain back-pressure on the solenoid valve. The solenoid valve was controlled from outside the MSC with a switch (Fig. 3). The flow rate was chosen to be around 11 ml s^{-1}, an intermediate rate between former comparable experiments by Conway et al. (2011) (c. 80 ml s^{-1}) and Massé et al. (2016) (c. 1–5 ml s^{-1}) and to minimize possible boundary effects (i.e. contact with the tray edges) under boiling conditions when erosion rates were high.

Temperature was monitored every second by 15 thermocouples (TCs) within and above the sand bed and in the water reservoir (Figs 2 & 3) with the following three configurations:

(1) Eight TCs on the floor of the tray along the centreline. The TCs were placed at 10 cm intervals and were then covered by sand. These TCs monitor the temperature at the interface between the metallic tray and the base of the sand bed.
(2) Four TCs placed at a 2 cm height within the sand bed. The support pillars were located at each corner of the test bed with distances of about 20 cm from the top and bottom and c. 8 cm from the lateral edges of the test bed (Fig. 2b). We used the average value of these four TCs to determine the average sand temperature.
(3) One TC placed just above the sand surface (c. 1 cm) at the centre of the right edge of the tray in order to measure air temperature close to the test bed. Furthermore, two other TCs were placed inside the water reservoir, to monitor the water temperature during the experiments.

We used two humidity sensors inside and outside the MSC respectively to monitor every 2 s the water vapour content (Fig. 3). Finally every experimental run was recorded with three cameras (Fig. 3): two webcams were placed in the interior of the MSC to record the front and the rear of each experiment, respectively, and one digital camera was placed outside of the chamber facing the tray through a glass window.

Experimental protocol

The sand, pre-cooled as necessary, was placed in the tilted tray inside the MSC and levelled. The test bed was photographed (at least 40 photos) using multiple observation angles in order to construct a high-resolution orthoimage and digital elevation model (DEM) of the surface by photogrammetry (see the section 'Mapping and quantification'). After this procedure, the MSC was evacuated. The experiment was started when the pressure reached c. 7 mbar and when the temperatures of the water and the sediment were at the desired values.

The solenoid valve was thereafter opened and the flow rate immediately adjusted so that the flow was as consistent as possible between experiments. The flow rate for experiments at Martian pressure was therefore set at a value around 11 ml s^{-1} (Table 3). The duration of the water flow was 60 s, leading to a total released volume of water between 610 and 690 ml (Table 3). After the end of the water flow the MSC was held at low pressure to observe the continuing infiltration of the water under realistic conditions. Then the MSC was finally decompressed and the test bed was photographed again with the same method as described above. Additional photos of interesting features were acquired at the surface of the test bed and of vertical cross-sections. The cross-sections were cut manually perpendicular to the slope direction. In order to not erase sedimentary structures within the vertical section, the sand was gently removed starting from the bottom of the tray and sections through the saturated material were broken off manually. Depending on the length of the saturated section we made between one and four vertical cross-sections.

Results

General observations

Tables 2 and 3 provides a summary of all parameters measured and results obtained for the experiments performed in this study. Representative examples of final surface morphologies of each sediment–water temperature combination are shown in Figure 4.

Videos recorded by the three cameras were carefully analysed in order to identify the physical processes, their timing and duration for any given experiment. We identified six distinct sediment transport processes that are detailed below. An overview of these event timings is given in Figure 5 and a quick description of the terminology used and the measurements performed are presented in Table 2.

Table 2. *Definition and related observations, measurements and analyses performed for different physical processes identified in experiments*

Physical process	Definition of process	Measurements, analyses and observations
Overland flow	Direct sediment transportation by liquid water flow	Mapping; Volumes of transported material; Length and width of flow feature; Description of morphology of overland flow feature (including cross sections); Formation speed of overland flow
Ejection of pellets	Saturated bodies of sediment roll/levitate over the surface	Mapping; Volumes of transported material; Duration of pellet production; Size, speed and trajectory of pellets; Description of morphology of pellets; Modelling of pellet levitation at terrestrial and Martian gravity; Calculations of gas production rate
Dry sand avalanches	Transportation of sediment without involvement of liquid	Mapping; Volume of transported material; Duration of dry avalanches
Percolation	Transportation, transformation and wetting of the surface by liquid water	Mapping; Volume of transported material and changes topographic relief; Description of texture and morphology of wet sand body (including cross-sections)
Sand ejection	Ejection of sand grain	Determination of grain ejection occurrence with videos; Duration of grain ejection; Modelling of sand grain ejection by gas flow at terrestrial and Martian gravity; Determination sand grain trajectory from high speed camera

Our results show that there are some physical events and processes that are common to all experiments and hence the resulting sand beds share similar surface features. For different combinations of sediment–water temperatures we also observed physical processes and morphological features specific to these combinations and these will be described in the sections 'Morphological differences observed as a function of sand temperature' and 'Morphological differences observed as a function of water temperature'.

For all of the experiments, we observed that the water boiled and persisted for enough time to flow over the surface and percolate into the sand. We made the following important observations:

(1) Once the sand was saturated close to the water outlet, we observed the formation of a feature created by overland flow of the boiling water (Figs 4, 5 & 6b, Supplementary videos 1, 2, 3, 4 and 5). The sand was eroded upslope by the water with the formation of an alcove, then transported by the water flow forming a channel that was still apparent at the end of the run, hence the name 'persistent channel', and accumulation occurred downslope (Fig. 6b). Small levees flanked these channels (Figs 6b, c & 7). Sediment transport and accumulation occurred through the deposition of a series of distinct sand lobes that extended incrementally downslope. The lobes generally superposed one another and sometimes

migrated laterally through time (Figs 6b & 7). The beginning of this 'overland flow feature process' was defined from the moment when the alcove at the top started to form and ended with the last observed deposition of sand transported by the water flow. The presence of cavities (around 2 mm) was observed in the persistent channel post-experiment (Figs 6c & 7), and those visible at the surface of the sand resulted from the burst of gas bubbles (Supplementary video 6). Cavities observed inside the channel are inferred to form by the same process. We found that it was quite common that a cavity is present at the end of a sand lobe, since the burst of the gas bubble seemed to stop the sand deposition (Fig. 6b). The construction of this channel-feature ceased synchronously with the end of the water release (Fig. 5).

(2) During all the experiments we observed the formation and the ejection of pellets from the water source area (Figs 5, 6a & 8, Supplementary videos 1–5). These pellets were saturated bodies of sediment. Their sizes range from about 0.5 to 60 mm with rounded and/or irregular shapes, and were observed to form when the boiling water interacted with the dry sand. The pellets slide and/or rolled downslope over the surface of the test bed and sometimes left a track in the loose sand (Fig. 6a). We defined this event as starting when the water

Table 3. *Summary of experimental parameters, measurements and calculations*

Run	Average sand temperature (K ± SD)	Average water temperature (K ± SD)	Average air temperature (K ± SD)	Average pressure (mbar ± SD)	RH (% ± SD)	Water flow amount (ml ± 5 ml)	Water flow rate (ml s⁻¹)	Total transported volume (cm³)	Details of transported volume (cm³)				Runoff length (cm ± 0.5 cm)	Runoff width (cm ± 0.5 cm)	Water vapour density ρ (kg m⁻³)	Threshold velocity U_t (m s⁻¹)	ΔP_{min} (Pa)	Ejection velocity U_e (m s⁻¹)
									Overland flow	Pellets	Dry avalanches/ saltation	Percolation						
S278-W278-1	278.5 ± 0.1	278.9 ± 0.1	285.5 ± 0.4	8.2 ± 0.5	22.5 ± 2.4	625	10.4 ± 0.4	86.1 ± 27.1	75.0 ± 7.6	0.6 ± 1.0	0.0	10.6 ± 18.4	38.1	7.6	6.9 × 10⁻³	6.3	73.4	0.01
S278-W278-2	278.5 ± 0.1	278.5 ± < 0.1	286.8 ± 0.1	8.4 ± 0.8	21.0 ± 3.5	670	11.2 ± 0.5	85.4 ± 20.3	71.1 ± 6.6	0.7 ± 0.9	0.0	13.7 ± 12.8	33.9	9.2	6.9 × 10⁻³	6.3	53.4	0.01
S278-W278-3	278.4 ± 0.1	278.7 ± < 0.1	286.1 ± 0.7	8.8 ± 0.7	–	665	11.1 ± 0.5	79.9 ± 7.1	72.7 ± 3.2	0.4 ± 0.2	0.0	6.8 ± 3.7	37.6	10.6	6.9 × 10⁻³	6.3	7.2	0.00
S288-W278-1	288.4 ± 0.1	278.4 ± < 0.1	292.8 ± 0.1	9.4 ± 1.4	18.3 ± 5.0	660	11.0 ± 0.5	446.7 ± 8.9	48.4 ± 4.7	35.9 ± 28.0	190.1 ± 28.0	172.3 ± 3.5	35.2	8.7	1.3 × 10⁻³	6.0	791.6	0.22
S288-W278-2	288.4 ± 0.1	278.6 ± 0.1	293.2 ± 0.5	10.0 ± 0.9	16.8 ± 4.7	655	10.9 ± 0.4	379.4 ± 11.7	45.4 ± 4.3	25.2 ± 20.2	168.2 ± 20.2	140.5 ± 4.3	34.7	7.0	1.3 × 10⁻²	6.0	731.6	0.20
S288-W278-3	288.1 ± 0.1	278.6 ± < 0.1	292.9 ± 0.1	9.3 ± 1.0	16.2 ± 5.0	650	10.8 ± 0.4	366.0 ± 7.8	47.5 ± 4.6	34.5 ± 20.4	177.2 ± 20.4	106.8 ± 2.4	34.4	7.2	1.3 × 10⁻²	6.0	768.5	0.21
S297-W278-1	296.5 ± 0.1	278.5 ± < 0.1	296.5 ± < 0.1	9.8 ± 1.1	–	620	10.3 ± 0.4	566.2 ± 25.5	25.8 ± 3.4	22.1 ± 15.2	292.4 ± 15.2	225.9 ± 8.4	26.1	7.8	2.1 × 10⁻²	5.7	1888.2	0.66
S297-W278-2	297.4 ± 0.1	278.7 ± < 0.1	297.4 < 0.1	8.7 ± 2.0	–	630	10.5 ± 0.4	806.6 ± 9.0	27.1 ± 3.1	96.3 ± 14.4	461.0 ± 14.4	222.2 ± 2.1	26.4	6.9	2.2 × 10⁻²	5.7	2157.8	0.77
S297-W278-3	296.4 ± < 0.1	278.4 ± < 0.1	295.6 ± 0.3	10.5 ± 1.5	20.8 ± 6.5	625	10.4 ± 0.4	846.9 ± 21.7	39.7 ± 3.2	86.8 ± 14.0	499.7 ± 14.0	220.7 ± 5.4	32.0	7.5	2.1 × 10⁻²	5.7	1800.9	0.63
S278-W288-1	276.8 ± 0.1	288.1 ± < 0.1	284.9 ± 0.2	8.9 ± 0.5	23.7 ± 5.2	–	–	58.7 ± 2.6	48.4 ± 1.1	0.3 ± 0.1	0.0	9.9 ± 1.4	27.6	10.5	6.2 × 10⁻³	6.3	−96.9	–
S278-W288-2	278.2 ± 0.1	288.3 ± < 0.1	286.7 ± 0.1	8.8 ± 1.0	24.1 ± 6.6	670	11.2 ± 0.5	87.9 ± 12.8	76.8 ± 5.0	1.0 ± 0.6	0.0	10.2 ± 7.2	31.9	8.1	6.8 × 10⁻³	6.3	−5.1	–
S278-W288-3	278.4 ± 0.1	288.4 ± < 0.1	286.3 ± 0.1	-	24.1 ± 6.9	650	10.8 ± 0.4	78.9 ± 27.4	68.5 ± 11.9	0.9 ± 1.3	0.0	9.5 ± 14.2	33.0	10.3	6.9 × 10⁻³	6.3	–	–
S288-W288-1	285.7 ± 0.1	288.2 ± 0.1	291.3 ± 0.1	9.5 ± 1.3	21.6 ± 6.5	650	10.8 ± 0.4	92.8 ± 7.7	29.4 ± 6.5	15.7 ± 10.5	32.4 ± 10.5	15.3 ± 3.4	29.1	9.0	1.1 × 10⁻²	6.1	503.0	0.13
S288-W288-2	288.9 ± 0.1	288.4 ± < 0.1	292.5 ± 0.1	10.0 ± 1.4	25.0 ± 8.2	660	11.0 ± 0.5	240.2 ± 42.9	40.2 ± 5.4	17.3 ± 10.7	121.8 ± 10.7	60.9 ± 13.6	27.7	7.4	1.3 × 10⁻²	6.0	788.0	0.22
S288-W288-3	288.1 ± 0.1	288.5 ± < 0.1	291.1 ± 0.1	9.7 ± 0.8	27.1 ± 7.2	665	11.1 ± 0.5	109.8 ± 34.1	50.7 ± 9.7	12.8 ± 8.1	18.5 ± 8.7	27.9 ± 16.3	33.5	8.6	1.3 × 10⁻²	6.0	728.5	0.20
S297-W288-1	296.0 ± 0.1	288.3 ± < 0.1	295.7 ± 0.2	10.1 ± 1.2	28.5 ± 9.3	660	11.0 ± 0.5	1011.5 ± 8.8	24.5 ± 5.2	204.2 ± 28.6	489.9 ± 28.6	293.0 ± 2.1	23.0	8.8	2.0 × 10⁻²	5.7	1772.7	0.61
S297-W288-2	296.1 ± 0.1	288.1 ± < 0.1	296.2 ± 0.2	9.7 ± 1.7	27.0 ± 8.3	670	11.2 ± 0.5	899.7 ± 17.5	26.9 ± 5.5	111.3 ± 17.7	551.6 ± 17.7	209.9 ± 3.9	22.0	8.7	2.0 × 10⁻²	5.7	1829.6	0.63
S297-W288-3	297.9 ± 0.1	288.4 ± < 0.1	298.2 ± 0.1	10.6 ± 1.7	26.2 ± 6.5	610	10.2 ± 0.4	1048.4 ± 8.5	21.2 ± 5.0	226.3 ± 30.2	528.5 ± 30.2	272.5 ± 1.7	20.8	8.3	2.3 × 10⁻²	5.7	2059.8	0.75
S278-W297-1	280.3 ± 0.1	296.3 ± < 0.1	287.9 ± 0.3	8.6 ± 1.6	28.1 ± 6.6	670	11.2 ± 0.5	74.7 ± 6.9	57.8 ± 2.4	0.7 ± 0.2	2.2 ± 0.3	14.0 ± 3.9	27.8	10.9	7.8 × 10⁻³	6.2	151.6	0.03
S278-W297-2	278.8 ± 0.1	295.8 ± < 0.1	286.0 ± 0.3	8.7 ± 1.2	29.2 ± 7.6	655	10.9 ± 0.4	72.2 ± 35.9	61.3 ± 14.3	0.7 ± 1.2	4.7 ± 3.8	5.4 ± 16.6	32.2	10.0	7.1 × 10⁻³	6.3	42.2	0.00
S278-W297-3	277.8 ± 0.2	297.4 ± < 0.1	285.5 ± 0.4	8.7 ± 0.9	32.4 ± 6.1	660	11.0 ± 0.5	57.5 ± 3.4	49.3 ± 1.1	0.3 ± 0.1	0.0	7.9 ± 2.1	29.8	7.5	6.6 × 10⁻³	6.3	−19.2	–
S288-W297-1	288.2 ± 0.1	296.4 ± < 0.1	291.6 ± 0.2	10.1 ± 1.0	32.7 ± 11.2	660	11.0 ± 0.5	133.2 ± 29.9	43.9 ± 6.8	12.2 ± 7.7	21.3 ± 7.7	55.8 ± 16.5	30.2	7.3	1.3 × 10⁻²	6.0	699.4	0.19
S288-W297-2	288.4 ± 0.1	296.3 ± < 0.1	292.5 ± 0.2	10.2 ± 1.5	29.5 ± 10.4	645	10.8 ± 0.4	173.6 ± 9.0	51.0 ± 7.7	15.2 ± 8.1	36.5 ± 8.1	70.9 ± 4.6	31.9	8.8	1.3 × 10⁻²	6.0	711.6	0.20
S288-W297-3	288.5 ± 0.1	296.4 ± < 0.1	293.1 ± 0.2	10.9 ± 1.2	26.1 ± 9.8	650	10.8 ± 0.4	162.8 ± 3.7	41.3 ± 6.5	19.4 ± 11.8	27.3 ± 11.8	74.8 ± 2.4	29.8	8.8	1.3 × 10⁻²	6.0	652.7	0.18
S297-W297-1	298.6 ± 0.1	301.7 ± < 0.1	300.4 ± 0.6	–	–	690	11.5 ± 0.5	815.3 ± 26.0	24.0 ± 5.6	131.0 ± 21.5	393.5 ± 21.5	266.8 ± 6.9	21.6	8.2	2.4 × 10⁻²	–	–	–
S297-W297-2	296.7 ± 0.1	296.6 ± < 0.1	296.6 ± 0.1	11.1 ± 1.7	28.0 ± 12.5	680	11.3 ± 0.5	649.1 ± 6.7	29.7 ± 5.1	46.2 ± 18.4	351.9 ± 18.4	221.3 ± 2.0	24.1	6.8	2.1 × 10⁻²	5.7	1793.0	0.80
S297-W297-3	297.8 ± 0.1	298.0 ± < 0.1	297.6 ± 0.2	10.1 ± 1.7	34.7 ± 12.8	680	11.3 ± 0.5	763.1 ± 6.7	22.2 ± 5.3	66.7 ± 19.1	522.4 ± 19.1	151.8 ± 1.5	21.6	7.8	2.2 × 10⁻²	5.7	2091.2	0.96

Temperatures, pressures and relative humidities (%RH) are presented as mean values and standard deviations (std) for the 60 s of liquid water release.

The details of error calculations for the reported volumes are given in the section 'Mapping and quantification'. The errors on water flow rate are calculated with the method of standard method of error propagation considering an incertitude of 2 s on the time. The details of the last four columns are given in the section 'Sand grain ejection'.
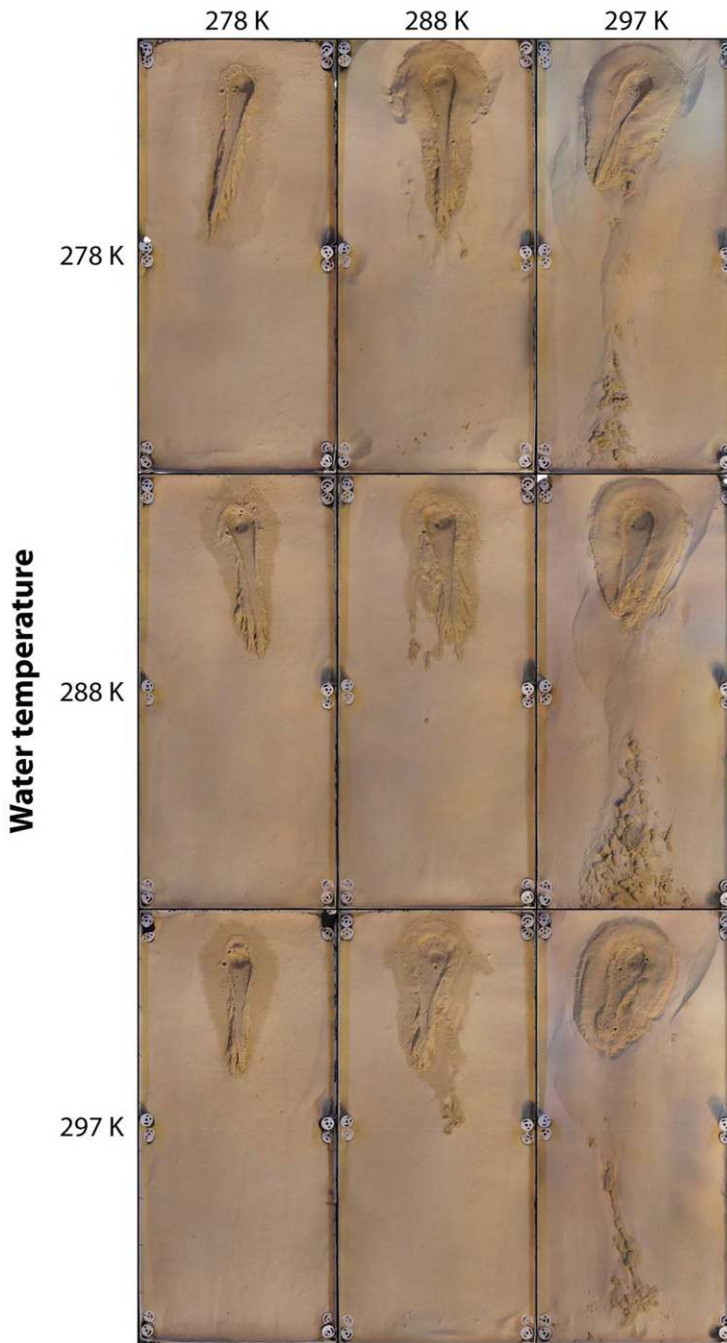
Fig. 4. Mosaic of typical morphological results obtained after the water flowed on the sand test bed as a function of sediment and water temperature. Orthoimages obtained by photogrammetry of the surface. The width of the test bed is about 40 cm. The top of the slope is located at the top of the image. The selected orthoimages correspond to the following runs: S278-W278-1; S288-W278-2; S297-W278-2; S278-W288-3; S288-W288-3; S297-W288-1; S278-W297-3; S288-W297-3; S297-W297-3 (from left to right and top to bottom).
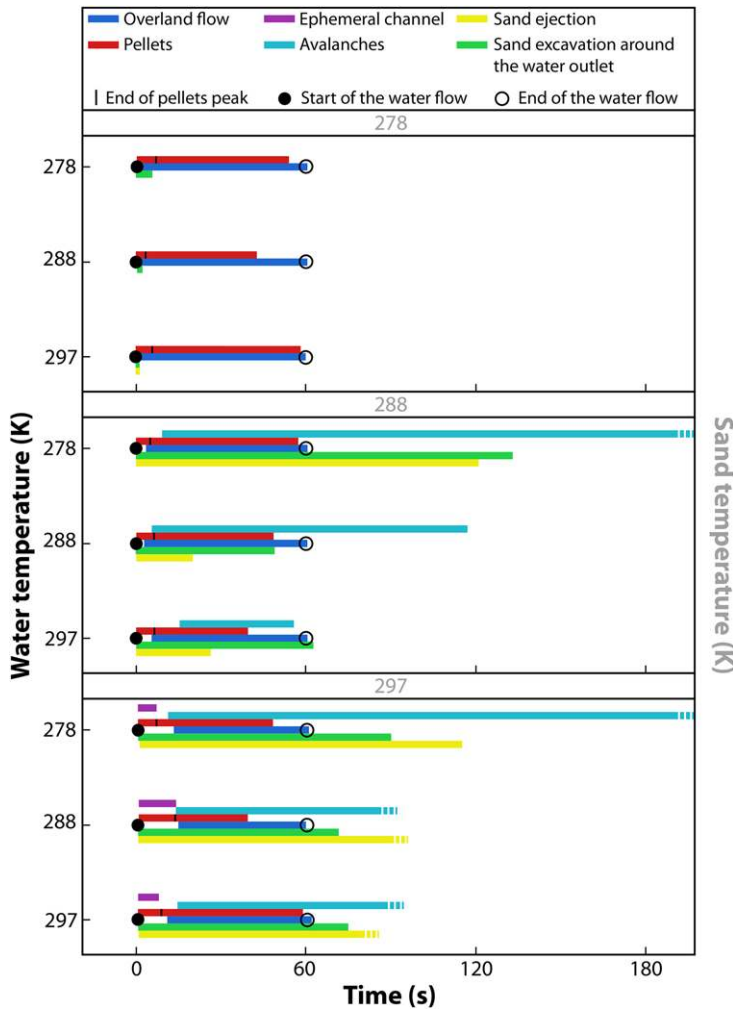
Fig. 5. Sequence of events as a function of sand temperature (grey labels at the top of each panel) and water temperature (black labels on *y*-axis). The length and position of the bars represent the average time from the triplicates for one T_s/T_w configuration. Dashed line indicates that the event is still active at the end for at least one triplicate. In this case, the unbroken line corresponds to the mean end time of the event or of the end of the video recording. The vertical black bar indicates the end of the peak period of pellet production.

first interacts with the sand and as ending when the last pellets come to a stop in the videos. These pellets are produced over the whole duration of the water release, but we generally observed that the peak in pellet production occurred in the first seconds of the experiments (Fig. 5). We defined the 'peak pellet' event in Figure 5 as starting at the production of the first pellet and ending when the production of pellets becomes sporadic with fewer than two pellets every *c.* 5 s.

(3) For some experiments we observed the formation of an ephemeral channel carved

into the dry sand by pellets moving downslope (Figs 4, 5 & 8, Supplementary videos 1 (right), 2 (right), 5 (right), 7 and 8). This channel was not visible or was poorly visible at the end of the experiments because it was generally backfilled with pellets and dry sand (Fig. 8). When this event occurred it was synchronous with the peak pellet event.

(4) Avalanches of dry sand were observed under certain conditions (Figs 4, 5 & 8, Supplementary videos 1 (right), 2 (right), 4, 5 (right), 9). We defined the duration of this event as
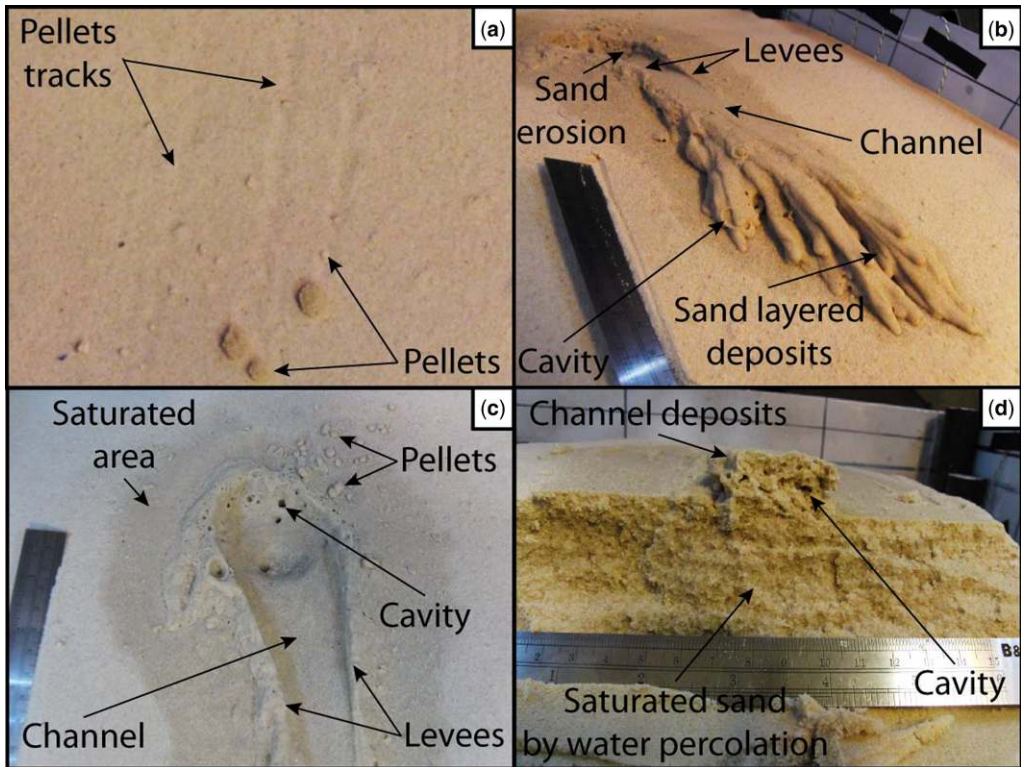
Fig. 6. Morphological features shared by all the experiments. (**a**) Rounded pellets (run S288-W278-2). They can create a track in the dry and loose sediments by rolling/sliding. The location of this image is outlined by the white box in Figure 8. (**b**) Persistent channel created by transport of the sand from the erosion area, situated mainly at the water outlet, to the accumulation area (run S278-W288-3). Levees are formed flanking the channel at the transition between these two areas. Accumulation of lobes of sand layers down flow, which often have cavities at their termini. The deposits are surrounded by a darker zone of saturated sand. The visible part of the ruler is about 10 cm long. (**c**) Water source area with gas cavities breaking the surface at the head of the persistent channel (run S278-W288-3). The infiltration of the water creates a darker saturated zone around the outlet and around the leveed channel. The visible part of the ruler is about 10 cm long. (**d**) Vertical cross-section of the test bed. (1) near the surface, the channel cross-section is elevated above the surface by the superposition of lobes (run S278-W297-3). The boiling water has created cavities in the sand. (2) The saturated zone observed at the surface is also visible at depth in the cross-section of the test bed. The visible part of the ruler is about 15 cm long.

being from the first avalanche to end of the last one in the videos.

(5) As the water was released we sometimes observed the ejection of individual sand grains at the saturated-dry boundary (Fig. 5, Supplementary videos 1 (right), 2 (right), 4, 5 (right), 9 and 10). We defined the beginning and the end of the ejection event by simply noting the first and the last (respectively) observations of sand ejection in the videos.

(6) For all the combinations of water and sand temperatures (but not for all the experimental runs), we observed the excavation of the dry sand around the water outlet creating a depression (Figs 5 & 7, Supplementary videos 1 (right), 2 (right), 4, 5 and 9). For most of these observations the excavation is clearly associated with dry sand ejection and granular avalanches. However, for three experiments (runs S278-W278-2, S278-W278-3 and S278-W288-3) no dry sand ejection could be identified from direct observation or from the video data. We attribute this inconsistency to natural variations in the sand compaction between experiments. We defined the start of this event as being when the water released interacted with the dry sand and the end when the edges of the depression excavated are not expanding anymore in the videos.

(7) Around the overland flow feature, the water continued to percolate even after the end of
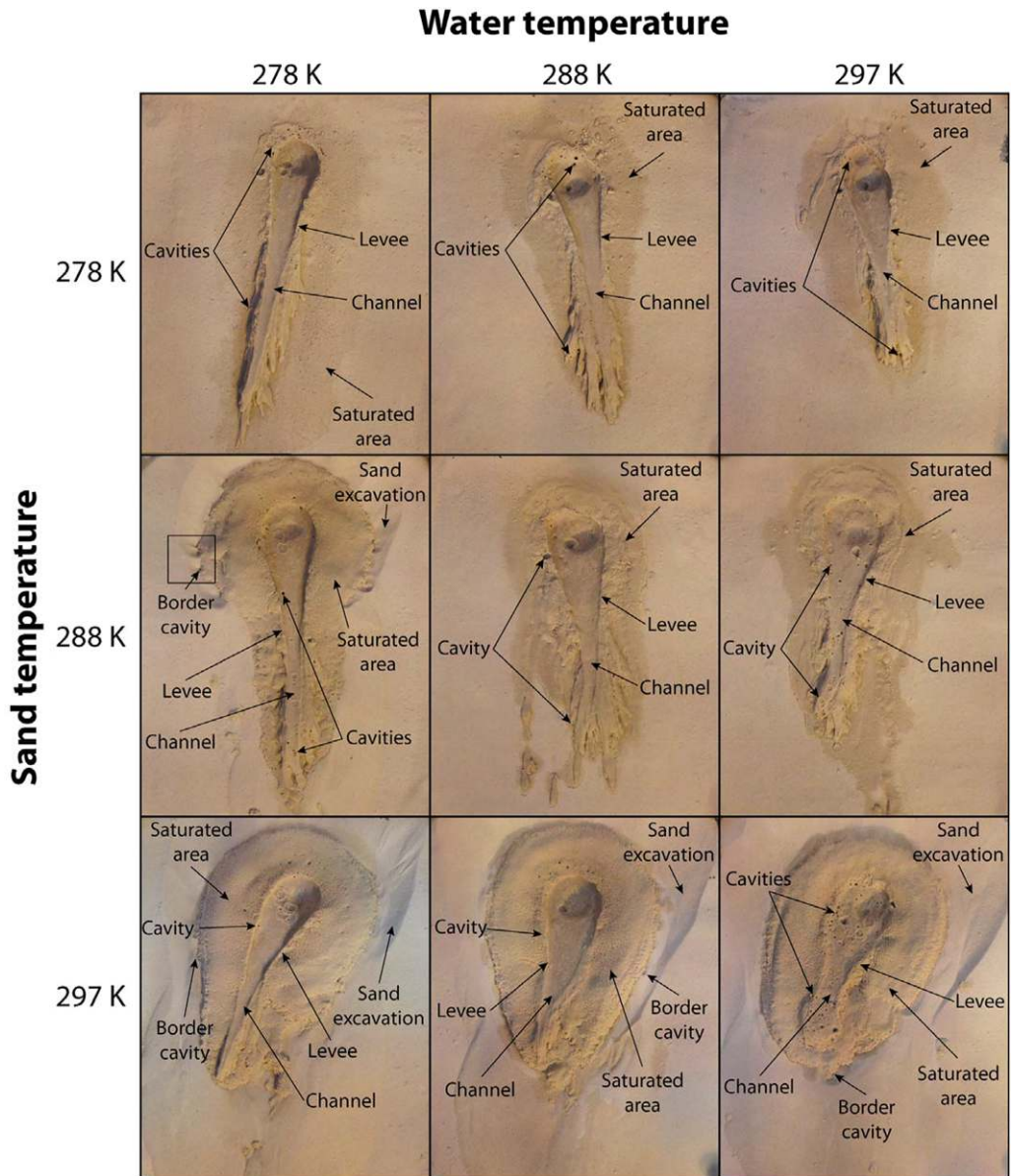
Fig. 7. Persistent channel morphologies as a function of sediment and water temperature with annotations. Orthoimages are obtained by photogrammetry. The width of the images is about 25 cm. The black box indicates the position of the zoomed image in Figure 10b. The selected orthoimages correspond to the following runs: S278-W278-1; S278-W288-3; S278-W297-1; S288-W278-2; S288-W288-3; S288-W297-3; S297-W278-2; S297-W288-1; S297-W297-3 (from left to right and top to bottom).

water release and a saturated zone of wet sand formed at the surface (Figs 4, 6c, d & 7, Supplementary video 5). This percolation is visible via a darkening of the sand. Vertically cut channel cross-sections all showed the same features (Fig. 6d): (a) near the surface there was a high porosity owing to the cavities formed by bubbles produced by the boiling water; and (b) below down to the base, the sand was wet owing to water percolation.
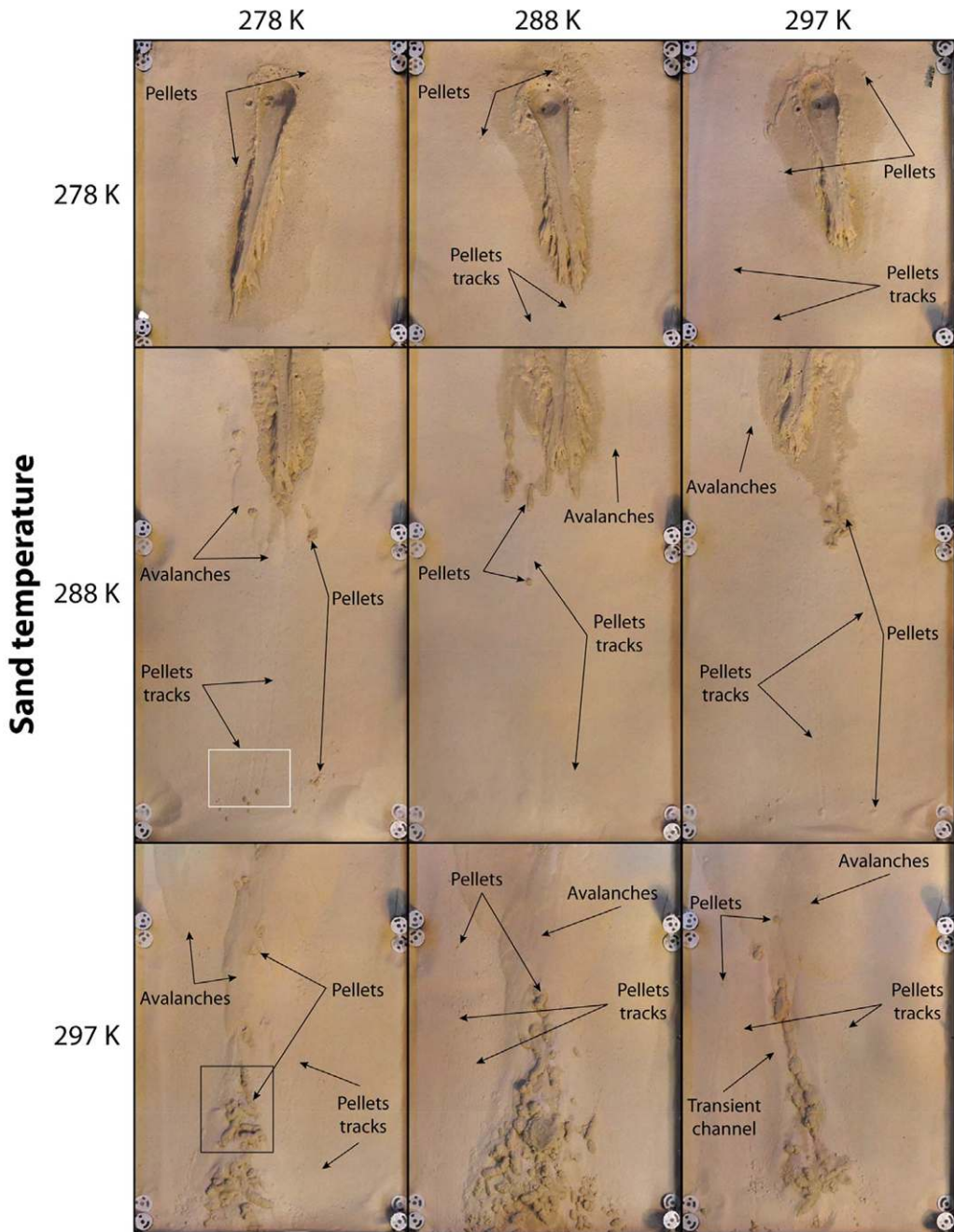
Fig. 8. A series of annotated images highlighting the morphological influence of the pellets as a function of sediment and water temperature. Orthoimages are obtained by photogrammetry. The width of the images is about 40 cm. Zoomed images in the white box and the black box are shown in Figures 6a & 10a, respectively. The selected orthoimages correspond to the following runs: S278-W278-1; S278-W288-3; S278-W297-1; S288-W278-2; S288-W288-3; S288-W297-3; S297-W278-2; S297-W288-1; S297-W297-3 (from left to right and top to bottom).

Morphological differences observed as a function of sand temperature

Here we describe how the morphology and the physical processes change owing to sand temperature. We describe only features common to all water temperatures for any given sand temperature. The description of the sequence of events is complemented by video screenshots at the different sand temperatures which are presented in Figure 9.

At a low sand temperature (*c.* 278 K), millimetre-size rounded pellets are ejected as the liquid water is released (Figs 5 & 9a [1–3]). They slide for *c.* 1 s and then stop or roll downslope (Supplementary
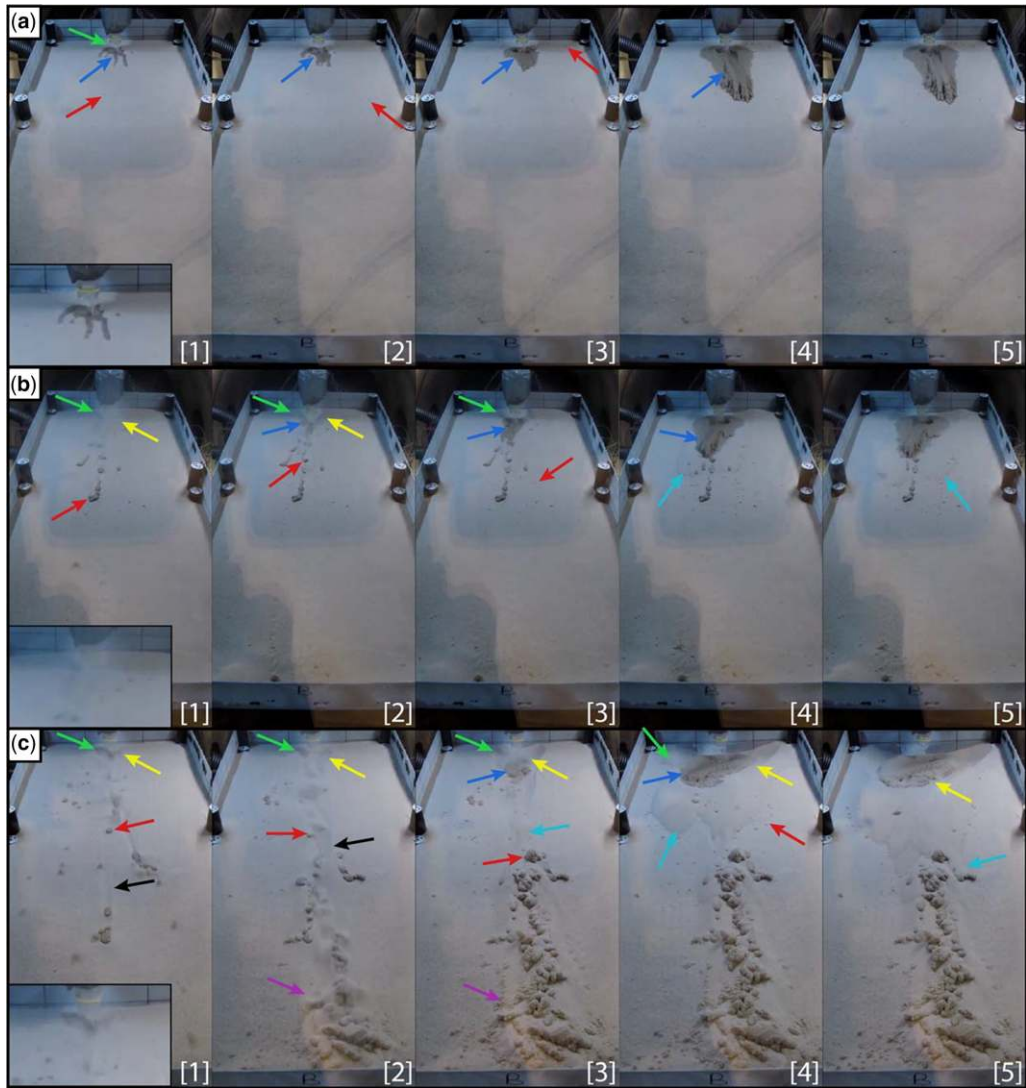

Fig. 9. Screenshots of videos for three sand and water temperature configurations at different times during the runs: [1] *t* = 2 s, [2] *t* = 5 s, [3] *t* = 14 s, [4] *t* = 60 s and [5] *t* = 92 s. The arrows indicate the events of interest that are occurring at the time of the screenshots: red arrows indicate pellet movements; yellow arrows indicate dry sand ejection; green arrows indicate sand excavation around the outlet; blue arrows indicate the formation of the persistent channel; light blue arrows indicate dry sand avalanches; black arrows indicate the channel carved by pellet-movement and purple arrows indicate the debris fan. For frame [1] an inset is included detailing the water outlet to highlight any sand ejection. (**a**) T_s = 278 K and T_w = 288 K (run S278-W288-3). (**b**) T_s = 288 K and T_w = 288 K (run S288-W288-2). (**c**) T_s = 297 K and T_w = 288 K (run S297-W288-2).
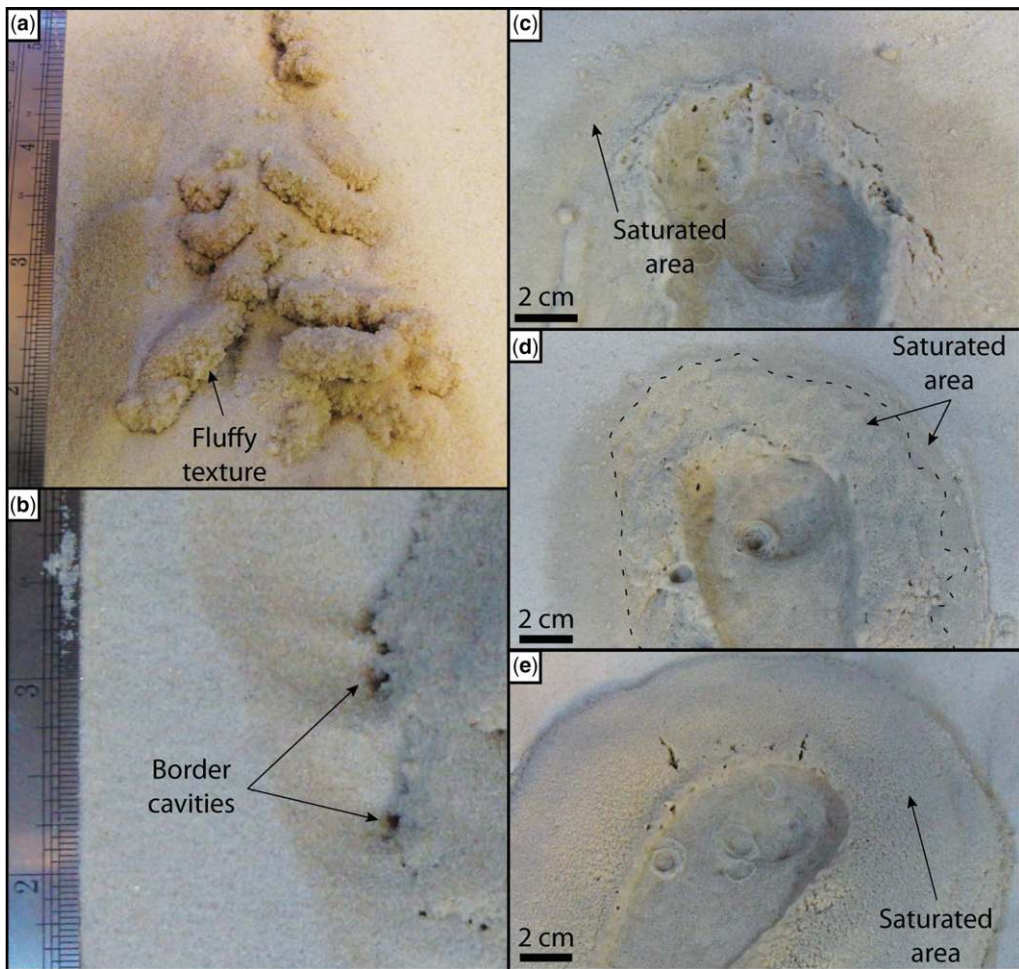
Fig. 10. Images of unusual morphological features observed following the experimental runs. (**a**) Centimetre-sized pellets present in a debris fan which have a fluffy sand texture at their base. The location of this image is shown by the black box in Figure 8 (run S297-W278-2). (**b**) Cavities produced by sand ejection owing to intense gas release at the boundary between water saturated sediment and dry sediment. The location of this image is shown by the black box in Figure 7 (run S288-W278-2). (**c**) Erosional area at the water outlet for a run at $T_s = 278$ K and $T_w = 288$ K (run S278-W288-2). (**d**) Erosional area at the water outlet for a run at $T_s = 288$ K and $T_w = 288$ K (run S288-W288-3). The black dashed line indicates the boundary between two different textures of saturated sand. The inner saturated zone had a fluffier texture than the outer saturated zone. (**e**) Erosional area at the water outlet for a run at $T_s = 297$ K and $T_w = 288$ K (run S297-W288-2). The area where water had infiltrated had a fluffy texture.

videos 1 (left), 2 (left), 5 (left) and 6), sometimes leaving tracks on the dry sand bed (Figs 6a & 8). The pellets numbered in the hundreds during the 60 s of water flow. Usually sand grain ejection did not occur at this sand temperature. We observed this process for a few seconds only in one run (Fig. 5, run S278-W297-2).

Sometimes (in five out of nine runs), a depression was formed by the transport of dry sand around the water outlet. This event is rapidly overprinted by overland flow and the extension of the saturated zone (Fig. 7 and Supplementary video 5 (left)).

A straight channel, constructed by transport of sediment by overland flow, started to form at the beginning of the water release and its formation stopped when the water valve was closed (Figs 5 & 9a [1–4], Supplementary videos 1 (left), 2 (left), 5 (left) and 6).

During all the experiments water percolated into the surrounding sand, forming a darker saturated zone of wet sand around the channel but with

no other obvious surface changes (Figs 6, 7 & 10c, Supplementary videos 1 (left), 2 (left), 5 (left) and 6).

For experiments performed at a high sand temperature (c. 297 K), we found additional processes and features. Pellets were also formed at the beginning of these experiments, when the water interacted with the dry sand (Figs 5 & 9c [1–4]). However, the range of sizes was larger than at 278 K, from millimetre to centimetre scale (0.5–60 mm), with irregular shapes and a fluffy texture at the base of the larger ones which developed during their formation and sliding (Fig. 10a). They slid and/or rolled downslope with a low direct contact with the surface of the test bed (Supplementary videos 1 (right), 2 (right), 5 (right)). The number of large pellets forming in the first few seconds of the water released was higher than at 278 K. These pellets carved a depression in the sand as they slid and rolled downslope, leading to the formation of a transportation channel about 5 cm wide with a curvilinear shape (Raack et al. 2017). As the pellets reached the bottom of the tray, the ephemeral channel was backfilled after a few seconds by more pellets and avalanching dry sand (Supplementary video 7). The duration of the pellet peak is similar at $T_s =$ 278 and 297 K, but in the last case the amount of transported sediment is greater (see the section 'Transported volume of sediment'). At the end of these experiments we counted several hundred pellets on the sand test bed.

As boiling water interacted with the sand bed, we also observed the ejection of dry sand grains. In the first second the ejected sand was continuous and intense (Supplementary videos 1 (right), 2 (right), 5 (right)). This stopped when the sand at the water outlet was saturated. The ejection process persisted after the end of the water release for tens of seconds (Fig. 5, Supplementary video 9). The ejection was therefore observed locally at the border between the saturated sand and the dry sand (Fig. 9c [4–5]), Supplementary video 9), sometimes leaving deep cavities (Figs 7 & 10b). Both the production of pellets and the sand ejection triggered avalanches of the dry sand. These avalanches extended downslope, covering the ephemeral channel and the previously deposited pellets. The avalanches continued to occur after the end of the water release, for several seconds or even minutes (Figs 5 & 9c [5], Supplementary video 9). We observed a greater lateral extension of the excavation of the sand around the source area (Fig. 5) than for $T_s =$ 278 K. The intense ejection of sand grains and avalanches favoured the growth of the depression that was not later overprinted by the overland flow and/or water percolation (Fig. 7). When the sand at the water outlet started to become saturated, the intensity of sand ejection reduced and a persistent channel was formed

by overland flow. These processes occurred about 20 s later than for the experiments at a sand temperature of 278 K (Figs 5 & 9c [3], Supplementary video 5 (right)). Finally, as at $T_s =$ 278 K, some of the water percolated into the sand and a saturated zone demarking the limit of water infiltration grew around the persistent channel. However, the texture of the wet sand appeared to be fluffier than it was at a colder sand temperature (Figs 7 & 10e). In addition, the imprint of the saturated zone was topographically highlighted by the removal of some of the loose dry sand around it.

The experiments at intermediate sand temperature ($T_s = 288$ K) displayed similar processes and morphology to the experiments at the other two sand temperatures. The pellets formed during these experiments had irregular shapes with sizes ranging from 0.5 to 30 mm. They formed in a limited amount (about 100) compared with the experiments at $T_s =$ 297 K (several hundreds). The centimetre-sized pellets slid over the sand but only over a very short duration (<1 s) and did not reach the bottom of the tray. The sand ejection had a shorter duration than at higher temperature (except at water temperatures $T_w = 278$ K). The avalanches of dry sand were smaller than at a sand temperature of 297 K. The excavation of the depression around the outlet was overprinted by the overland flow and water percolation (Fig. 7, Supplementary video 4). The persistent channel formed by the overland flow started to form a few seconds after the beginning of the experiment (Fig. 5). The saturated zone around the persistent channel either had the fluffy, high-relief appearance of ones formed at higher temperature (at $T_w =$ 278 K) or an intermediate morphology. In some experiments we observed that the saturated zone displayed two different textures and topographic expressions depending on its radial position (Fig. 10d). The wet sand in contact with the persistent channel (inner saturated zone) was rough, with a sand texture looking less 'cohesive' than at colder temperatures and in some places fluffy. The outer saturated zone of wet sand, in contrast, showed no unusual texture, similar to the saturated zone in the colder experiments.

Morphological differences observed as a function of water temperature

If we compare experiments performed at different water temperatures yet with the same sand temperature, only slight differences can be found. As in the preceding section, we describe how the morphology and the physical processes change and we describe only features common to all sand temperatures for any given water temperature. An increase in water temperature tends to decrease the runout length of

the overland water channel (Fig. 4 and the section 'Overland flow feature').

At a sand temperature of 278 K, we noted no significant influence of water temperature on the sequence or duration of events. At $T_w = 298$ K, dry sand ejection occurred for a few seconds at the beginning of one of the experiments (Fig. 5, run S278-W297-2) and hence may not be representative.

However, at a sand temperature of 288 K, water temperature affected both physical processes and surface morphologies. The duration of the dry sand avalanches and the sand ejection tended to increase between $T_w = 297$ K and $T_w = 278$ K (Fig. 5). Avalanche events occurred at least 60 s later at $T_w = 288$ K compared with $T_w = 297$ K, and at $T_w = 278$ K compared with $T_w = 288$ K, and the ejection of the sand grains had a duration of up to two times longer at $T_w = 278$ K than at higher temperatures. The observed surface morphology of the overland flow and the water saturated zones was also different depending on the water temperature. Features at $T_w = 288$ K and $T_w = 297$ K were similar (Fig. 7), both having a saturated area characterized by a rough inner part with a darker colour and fluffier sand texture and an outer part with only an albedo difference, few pellets and small sand avalanches (Fig. 5). At $T_w = 278$ K, the saturated area had a convex topographic surface and a fluffy texture. These resembled the saturated area observed at $T_s = 297$ K (Fig. 7). The top of the saturated area was also surrounded by a sand excavation hole (Fig. 7). For runs at $T_w = 278$ K, we observed a depression created by the ejection of sand grains at the boundary of the saturated area, a feature which was not present at higher temperature. Finally, avalanches were more numerous and larger at $T_w = 278$ K than at higher temperature.

At sand temperature of 297 K we did not inventory any morphological changes which can unambiguously be attributed to changes in water temperature alone. Although the duration of the ejection and avalanches seemed to follow a similar trend to experiments at $T_w = 288$ K (the duration increased as the water temperature decreased), some of the videos were stopped before the end of these events (runs S297-W297-3 and S297-W288-2, Fig. 5), so this observation remains ambiguous.

Analysis methods

Mapping and quantification

Photos of the test bed acquired before and after the experiments were used to produce orthophotos and DEMs. The photos were processed with Agisoft PhotoScan Professional software, which produces 3D models of a scene using multiview photogrammetry, otherwise known as 'structure-from-motion'

(Westoby *et al.* 2012). We produced orthophotos with 0.2 mm spatial resolution and DEMs at 1 mm spatial resolution of the sediment beds. To ensure the resulting models were at the correct scale, to reduce distortion and so that before-after pairs were correctly coregistered, we included 12 black and white targets, 2.7 cm in diameter, with known relative positions in the processing (Figs 2b & 3).

The obtained data were then exported to ArcGIS software and three types of measurements were performed (Table 2): (1) mapping of the spatial domains of the different flow processes; (2) volume measurements of erosion and deposition (transported material); and (3) manual measurements, including length and width of the channel (Table 3). Each of these is described in more detail below.

(1) We mapped the area affected by the different flow processes at the end of the experiments using the orthophotos, DEM and a relief-shaded version of the DEM (termed as hillshade model henceforth) with reference to the processes visible in the videos. Following Raack *et al.* (2017) the extent of the processes was identified (Fig. 11) in line with the description of processes given in the section 'General observations' (Fig. 5, Table 2): (a) in blue, the overland flow feature; (b) in red, pellets that form with liquid water contact and move downslope by rolling/sliding; (c) in yellow, dry processes including sand ejection and dry avalanches; and (d) in green, areas where substrate was affected by water percolation.

(2) Based on our manual mapping of the surface expression of each transport mechanism, we made an estimate of the volume of sediment transported by each of these mechanisms (Tables 2 & 3). To calculate the volume of sand eroded and deposited, we combined the region mapping with the calculation of the elevation changes between DEMs before and after the experiments (Fig. 12). This method of estimating the volume relies on the assumption that the final morphology is representative of the cumulative transport via these processes throughout the experiments. However, these processes superpose in space and time, meaning the volumes of these particular transport processes we calculate from our mapping remain relatively crude estimates. For example, we observed that pellets deposited early in the experiment could be superposed by dry avalanches, and erosion could be performed by both pellet ejection and dry avalanches/ejection and overland flow, yet finally was mapped as overland flow. We followed the methods employed by Raack *et al.* (2017) to place reasonable uncertainties on our estimated
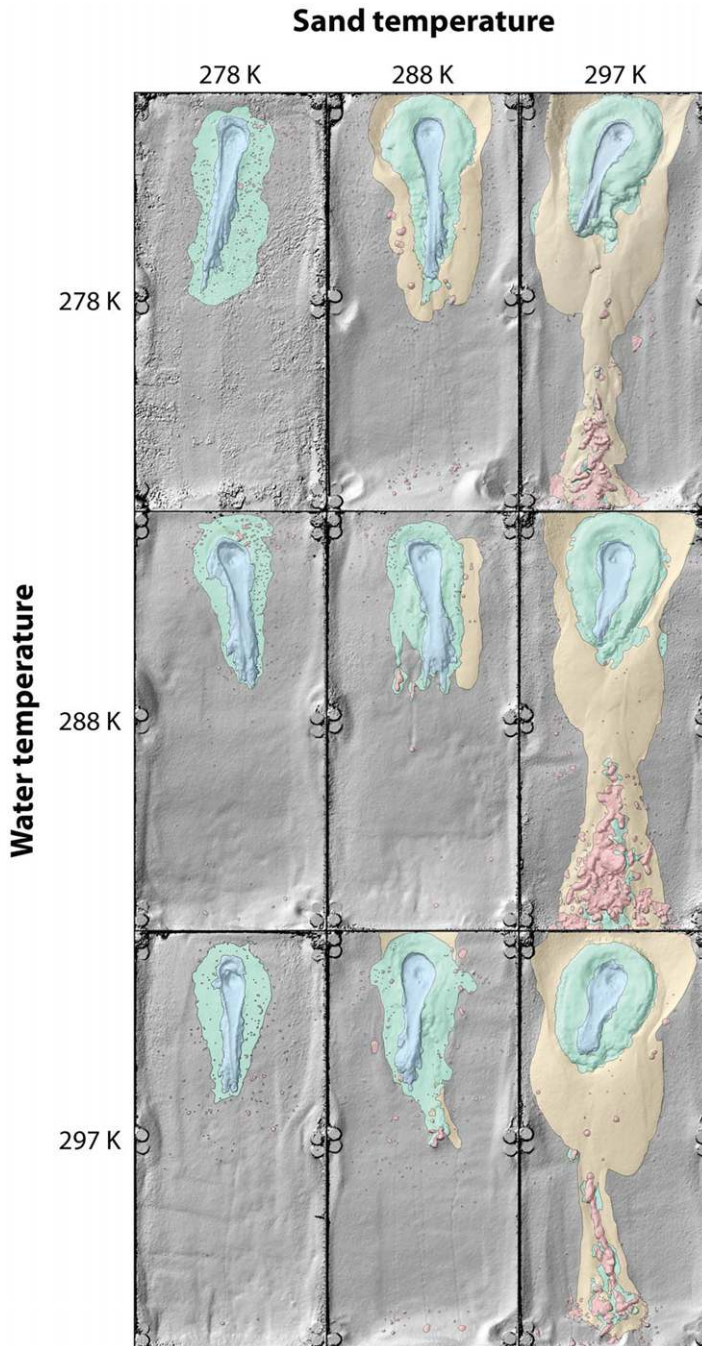
Fig. 11. Mosaic of morphological maps obtained after the water flowed on the sand test bed as a function of sediment and water temperature. The mapping highlights the area affected by different transport processes (blue = overland flow, green = percolation, red = pellets, yellow = dry avalanches/ejection). The maps are overlain on a hillshaded relief model generated from digital elevation models (1 mm/pix) obtained by photogrammetry. The width of the test bed is about 40 cm. The top of the slope is located at the top of the image. S278-W278-1; S288-W278-2; S297-W278-2; S278-W288-3; S288-W288-3; S297-W288-1; S278-W297-3; S288-W297-3; S297-W297-3 (from left to right and top to bottom).
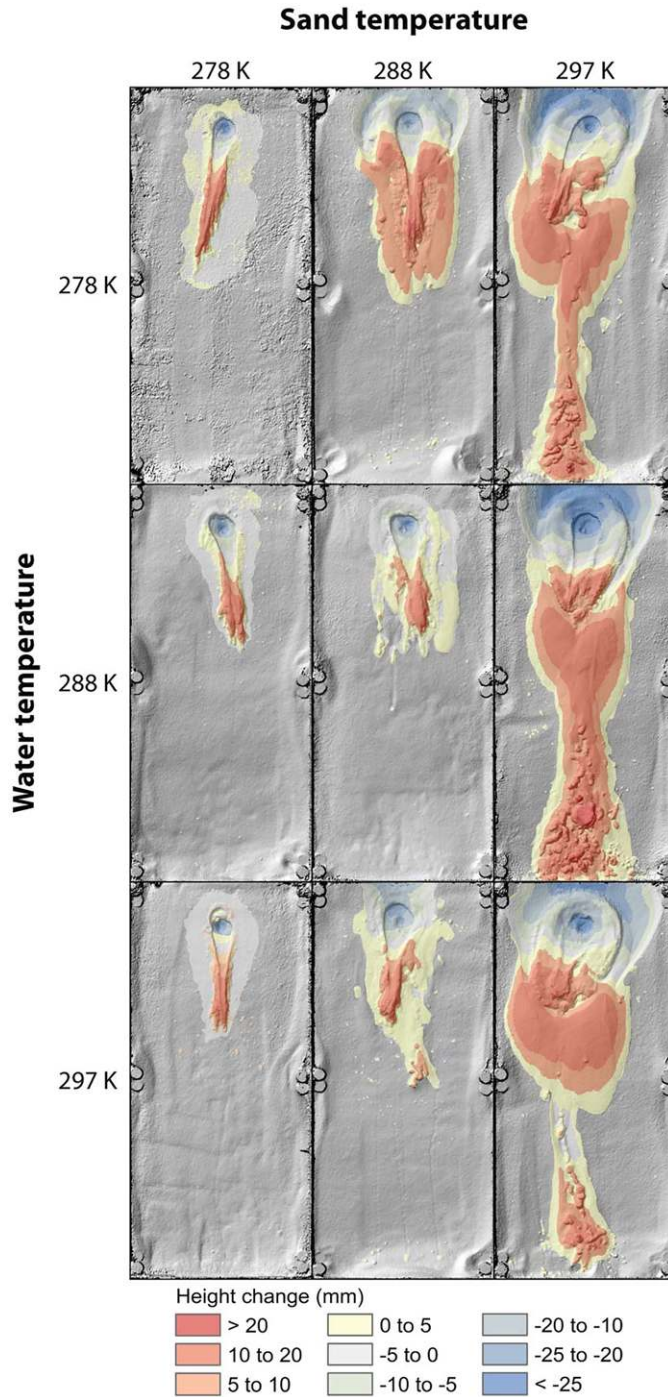
Fig. 12. Mosaic of the elevation difference between start and end of experiments as a function of sediment and water temperature. The elevation differences are overlain onto a hillshade relief model derived from the DEMs (1 mm/pix) obtained by photogrammetry. The width of the test bed is about 40 cm. The top of the slope is located at the top of the image. S278-W278-1; S288-W278-2; S297-W278-2; S278-W288-3; S288-W288-3; S297-W288-1; S278-W297-3; S288-W297-3; S297-W297-3 (from left to right and top to bottom).

volumes. The total errors for eroded, deposited and the resulting transported volume (Table 3) were calculated with the 'measurement error' which was scaled by their respective surface areas. To give a more precise classification of the transported material into our chosen transport mechanisms (overland flow, percolation, pellets and dry avalanches/ejection) we also calculated the 'superposition error' and the 'interpolation error'. These errors had no influence on the total error of each experiment ('measurement error'), but appeared in the subdivision for each transport mechanism (Raack *et al.* 2017).

The 'measurement error' ranged from 0.1 to 22.6 cm^3 (with a median value of 2.1) for individual transport mechanisms, and from 2.6 to 42.9 cm^3 (with a median value of 9.0) for total error. For each experiment we performed volume calculations on undisturbed surfaces (not affected by flows, pellets and/or avalanches) on a fixed area of *c.* 46 cm^2 to estimate our measurement error. The resulting volumes were scaled to the areas of the transportation mechanisms or the total area, as appropriate. This approach was used because many factors influence the errors in DEMs (e.g. quality of photos, misplacement of targets, light differences, etc.), which are individually hard to estimate, vary from experiment to experiment and influence the calculation of volumes.

The 'superposition error' ranged from 7.7 to 30.2 cm^3 (with a median value of 16.4) and was calculated as follows. From our observations for experiments at intermediate (288 K) and warm (297 K) sediment temperatures, we found that the area which was mapped as overland flow was also affected and eroded by pellet ejection and dry avalanches/ejection during the first seconds of water released. During experiments at low sediment temperatures (278 K) this effect was not observed. Therefore to avoid an overestimation of the overland flow erosion volume for the experiments at 288 and 297 K sand temperature, we made an adjustment to our usual calculations. Instead of using the 'before' DEM for volume calculations (volume = difference between 'before' and 'after' DEMs), we used an interpolated 'natural neighbour' surface DEM fitted to elevations extracted from the 'after' DEM within a 2 mm buffer outside the digitized boundary of the overland flow. Using this new surface meant that we did not include the material eroded via pellet ejection and dry avalanches/ejection earlier in the experiment. We assigned this volume to the overland

flow category, but this left us with a remnant volume which had no assigned process. We observed in the videos that this material was transported by pellet ejection and dry avalanches/ejection; therefore we partitioned it arbitrarily 50–50% to both of these mechanisms. We do not know the exact partitioning so therefore we assume this 50% remnant volume to be the worst-case uncertainty on the volume partitioning.

The 'interpolation error' ranged from 3.1 to 7.8 cm^3 (with a median value of 5.2). As a second step, we calculated the uncertainty on using the natural neighbour method to estimate the original basal surface (as described in the 'superposition error' above). For this, we used the above-described methods to calculate the volumes for overland flow for cold experiments (278 K), using both the interpolated and 'before' basal surface, but this time we knew that this zone was not affected by other mechanisms. The difference between these calculations was taken as the 'interpolation error'. The gathered values were averaged for experiments with the three different water temperatures. We then scaled this uncertainty for the area of overland flow for intermediate and warm experiments.

(3) We used the DEM and orthophotos to measure the linear dimensions of pertinent features, as follows. The length of the overland flow feature (Table 3) was defined as the maximum linear distance between the uppermost sediment disturbance and the lowermost sediment disturbance caused by direct entrainment by liquid water. The width of the overland flow feature (Table 3) was defined as the maximum linear distance between the outer edges of the levees resulting from overland flow taken perpendicular to the length measurement. The uncertainty on these measurements is *c.* 0.5 cm. Finally the average sizes of pellets were estimated by averaging their maximum and the minimum dimensions in plan view. The uncertainty is estimated to be *c.* 0.5 mm.

Speeds

The influence of the temperatures on the dynamics of the physical processes was investigated by computing the speeds of formation or displacement of key morphological features. The speed of formation of the overland flow feature was estimated using its measured length (see the section 'Mapping and quantification') and the duration of the formation of this feature (see the section 'General observations'). The estimated error on the duration was

1 s. For this calculation, the error on the speed was determined by error propagation of the errors on length and duration.

We also determined the speed of single pellets using the video by taking advantage of the graduations on the side walls of the tray (at 10 cm intervals). The mean propagation speed of the pellets was calculated by identifying the time at which the pellet reached the position 10 cm from the top of the tray to the position where it stopped.

Analysis results

Transported volume of sediment

We identified four different transport processes in our experiments which are also shown in our mapping: (1) overland flow; (2) ejection of single sand grains; (3) formation of pellets; and (4) dry avalanches (Tables 2 and 3 and Fig. 11). We found that the total volume transported (Figs 12 & 13) did not vary systematically with water temperature (Fig. 13a). However for $T_s = 288$ K the total transported volume decreased significantly (about two times less) between $T_w = 278$ K and the higher temperatures. This trend was not observed for $T_s = 278$ K or 297 K. This decrease could be linked with changes of the observed process dynamics (Fig. 7) of these experiments ($T_s = 288$ K and $T_w = 278$ K). We observed at $T_s = 288$ K and $T_w = 278$ K that the dry processes (sand ejection and avalanches) were more frequent and had a longer duration than at higher water temperature (Fig. 5 and Supplementary video 4) providing an explanation for the increase in sediment transport.

In contrast, we find that the total transported volume of sediment (Figs 12 & 13) systematically increased as the temperature of sand increased (Fig. 13b). The transported volume was about 9 times higher at 297 K compared with at 278 K, as was observed previously by Raack *et al.* (2017). At low sand temperature (278 K) most of the sediment was transported by entrainment of the sand by the flowing boiling water (*c.* 98%), while a limited amount (*c.* 2%) was transported in the form of wet sand pellets (Table 3). Sand ejection and avalanches were either not observed or transported negligible volumes. At higher temperatures, the balance of processes shifted (about 95% of sediments are transported by pellets and dry processes), as discussed previously (see the section 'Morphological differences observed as a function of sand temperature'), and this shift increased the amount of sediment transported. The absolute (and relative) volume of sediment transported directly by boiling water decreased as the sand temperature increased (Fig. 13c). This can easily be accounted for: first, the duration of the overland flow decreases with increasing temperature (Fig. 4). Second, the frequency of pellet production and dry avalanches increases with increased sand temperature. These two classes of sediment transport have an 'exponential-like' increase in volume with sand temperature (Fig. 13b). Together they constitute about 93–97% of the total transported volume at $T_s = 297$ K (Table 3). Therefore, the rapidly increasing trend of transported volume with sand temperature can almost entirely be accounted for by an increase in the intensity of pellet production and dry processes. The substantial increase in the volume of sediment transported can be attributed to the enhancement in the intensity of boiling experienced by the liquid water. This boiling intensity depends primarily on the sand temperature, rather than on the water temperature (Fig. 13b).

Overland flow feature

Increases in both water temperature and sand temperature tended to decrease the overall length of the overland flow feature (Figs 7 & 14). The length of the overland flow feature changed very little between water temperatures of 288 and 297 K and increased at 278 K (Fig. 14a). This increase may be linked to a slightly higher flow propagation speed for runs at $T_w = 278$ K compared with the other two (on average, 0.59 ± 0.01 cm s^{-1} at $T_w = 278$ K and about 0.49 ± 0.01 cm s^{-1} at $T_w = 288$ and 297 K; Fig. 15a). The reason for this higher speed, and therefore the longer length, could be that there is less water available at the surface at water temperatures ≥ 288 K. Our hypothesis is that the water percolates faster into the sand at warmer temperatures, decreasing the availability of water at the surface and/or that water needs first to change phase to cool down to reach the boiling point (latent heat), diminishing the amount available water (see more details in the section 'Sand and water temperature').

The lengths of the overland flow feature were similar at $T_s = 278$ and 288 K and decreased at $T_s = 297$ K (Fig. 14b). The flow propagation speeds were similar for all sand temperatures and did not show any trend (Fig. 15b). The shorter length of the overland flow feature at 297 K can be attributed to the later start of channel formation compared with experiments performed at lower sand temperatures (about 20 s later; Fig. 5). We think that this later start is due to the increased intensity of sand ejection and pellet production that inhibits/retards the saturation of the sand at the source area and so the initiation of the overland flow feature. The decrease in the transported volume by overland flow with increasing sand temperature is also linked to the reduction in the length of the overland flow feature (Fig. 13c).
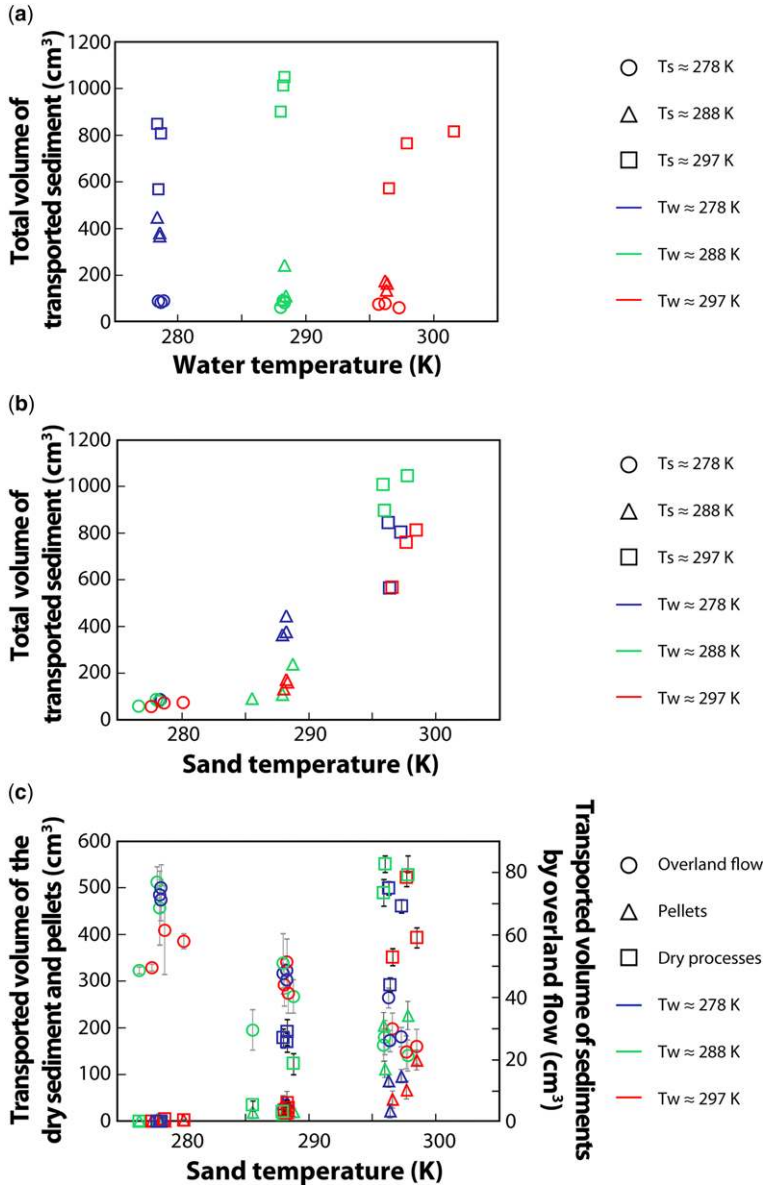
Fig. 13. Transported sediment volume v. temperature. The error values are presented in Table 3 for clarity (they fit within the points). (**a**) Total volume v. water temperature. (**b**) Total volume v. sand temperature. (**c**) Transported volume v. sand temperature, split into the different transport processes described in the section 'Mapping and quantification'.

Percolation

The saturated area of sand formed by percolation of the liquid water can have different surface characteristics (Fig. 10). At low sand temperature the water percolated into the sand, as revealed by the change of colour of the wet sand compared with its surroundings, with change in relief (Fig. 10c), while at a sand temperature of 297 K the surface of the saturated area had a fluffier sand texture and the boundary of the saturated area had topographic relief (Fig. 10e). We attribute this difference
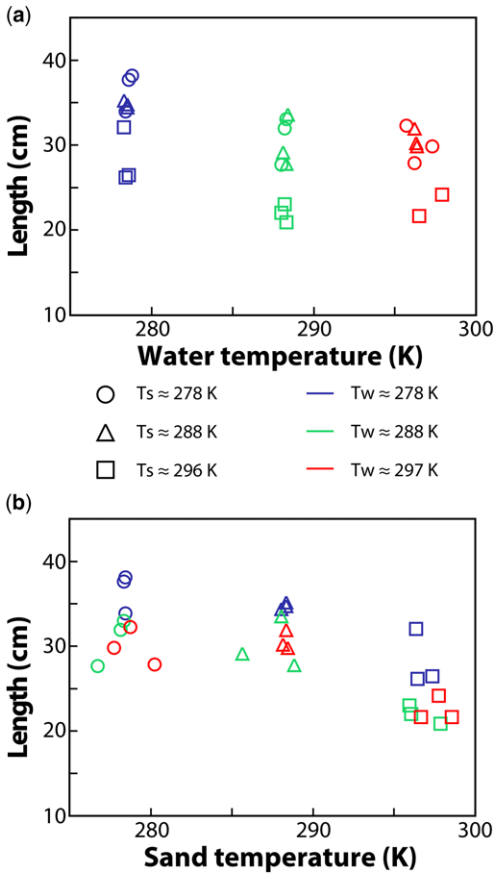
Fig. 14. Length of overland flow feature v. sand and water temperatures. (**a**) Water temperature. (**b**) Sand temperature.

Wet sand pellets

Pellet production was intensified at higher sand temperatures (Fig. 13b). At the highest sand temperature large numbers of pellets were formed, with sizes that could reach several centimetres and have irregular shapes (Figs 4, 9 & 10a). Water temperature did not have an influence on the number of pellets, their sizes or shapes (Figs 9 & 13a), or their average speed (Fig. 16a). Their average speed did increase with increasing sand temperature (Fig. 16b). From direct observation and the videos we note that the pellets formed at $T_s = 297$ K were more likely to slide rather than roll, which is generally the case at lower sand temperatures (Supplementary videos 1, 2, 3, 5, 6 and 7). We hypothesize that the sliding behaviour is caused by the formation of an air cushion at the bottom of the pellets (Raack *et al.* 2017). The gas produced by the boiling of water at the surface of the pellets is able to provide lift. The rate of gas production is enhanced by the increase in sand temperature (calculations predict about 5 times higher at 297 K compared with 278 K; Raack *et al.* 2017). Therefore pellets at $T_s = 297$ K go downslope faster compared with pellets at $T_s = 278$ K, partly owing to increased lift and a reduction in the friction force. Pellets which are lifted off the surface for a prolonged duration (several seconds) usually have a flattened shape, with larger surface area at the base compared with on their lateral faces (Fig. 10a). This flattened shape probably sustains the sliding movement for longer than would be the case otherwise, because it increases the surface area producing gas in the downward direction. Our hypothesis that gas is preferentially produced at the basal surface of the pellets is supported by our observation that pellets often have a fluffier texture on this surface (Fig. 10a). The unstable water also interacts with the sand and modifies sand cohesion and colour.

Dry processes

Sand ejection. The sand ejection is mainly associated with experiments at sand temperatures ≥288 K. For these experiments we assume that the production of water vapour is sufficiently intense to yield a gas speed able to entrain sand particles (detailed below in the section 'Sand grain ejection'). While the water is percolating through the sand, it comes into contact with relatively hot, dry sand and this contact causes rapid and sudden boiling of the water. If this occurs at the surface either at the dry-saturated boundary or because sand avalanches uncover this boundary, the boiling causes localized gas production that can move sand grains (Fig. 10b). The gas ejection is intense during the first few seconds following water release forming a depression around the saturated sand (Fig. 4).

to the intensity of boiling. We hypothesize that at $T_s = 297$ K the boiling-related phenomena are enhanced and the water that percolates into the sand undergoes a more energetic phase change process than at 278 K. Therefore, we think that the escaping gas velocity could be strong enough to move the grains of sand, increase the porosity and hence alter the texture and the topographic signature of saturated sand body at 297 K. At intermediate sand temperatures, both textures of the saturated area coexist and are adjacent (Fig. 10d). The fluffy texture was located proximal to the overland flow area, and we infer that the intensity of boiling is higher close to this area and so disturbs the texture of the sand. As the water percolates into the sand, we infer that it stabilizes, until the percolation of the water does not affect the texture of the sand but just darkens it.
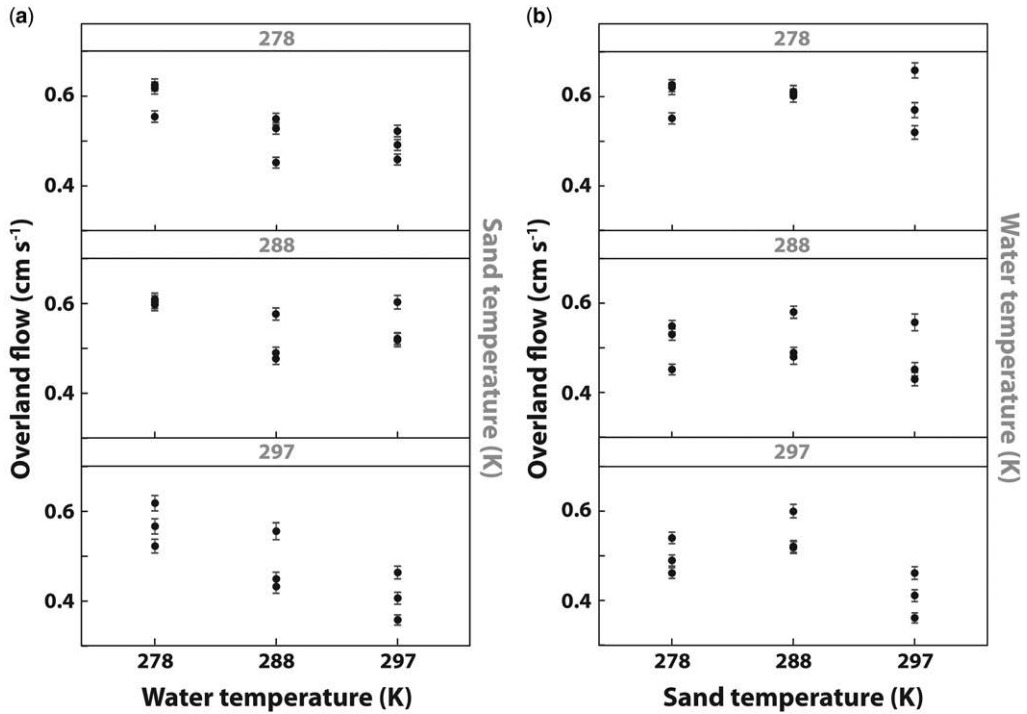
Fig. 15. Propagation speed of the overland water flow v. the water and sand temperatures. (**a**) Water temperature; (**b**) sand temperature.

Grain ejection can persist after the end of the water release (Fig. 5 and Supplementary video 9), indicating that the sand is supersaturated and that liquid water continues to percolate. The production of gas seems to be driven by the contact between the liquid water, air and hot dry sand ($T_s \geq 288$ K). Figure 17 shows that the duration of the ejection event is positively correlated with the difference in temperature ($\Delta T = T_s - T_w$) between the sand and the water. When $\Delta T < 1$ the ejection process either does not occur or is limited, whereas when $\Delta T > 1$ the duration of the process increases with increased ΔT. Therefore, the duration of the ejection depends on two parameters, the temperature of the sand that drives the sand ejection (see the section 'Sand grain ejection') and the water temperature that is thought to influence the amount of water available for liquid water flow and percolation into the sand (see the section 'Sand and water temperature').

Avalanches. Dry granular avalanches were observed only for experiments performed at sand temperatures ≥ 288 K, similar to sand ejection (Fig. 5, Supplementary videos 1 (right), 2 (right), 4, 5 (right) and 9). After the peak in pellet productions (Fig. 5), sand avalanches were mainly triggered at the boundary

between the saturated and dry sand, where the gas production was intense and destabilized the sand bed. For some experiments, we observed that grain avalanches continued after the liquid water release and ejection had stopped (Fig. 5). We inferred that, although the water was not visibly boiling anymore, it was still undergoing evaporation and even this low volume of escaping water vapour could destabilize dry sand close to the angle of repose.

Discussion

Sand and water temperature

Our results reveal that the physical events occurring during the experiments and the final surface morphologies of the sand bed strongly depend on the sand temperature (Figs 4, 5 & 13b) and only weakly on the water temperature (Figs 4, 5 & 13a). Sand ejection and dry avalanches are limited to experiments at sand temperatures ≥ 288 K (Fig. 5). In addition, the intensity of some processes is enhanced at increased sand temperatures, for example pellets are larger and more numerous, while persistent channel formation related to overland water flow is inhibited (Fig. 5). The combination of these factors results
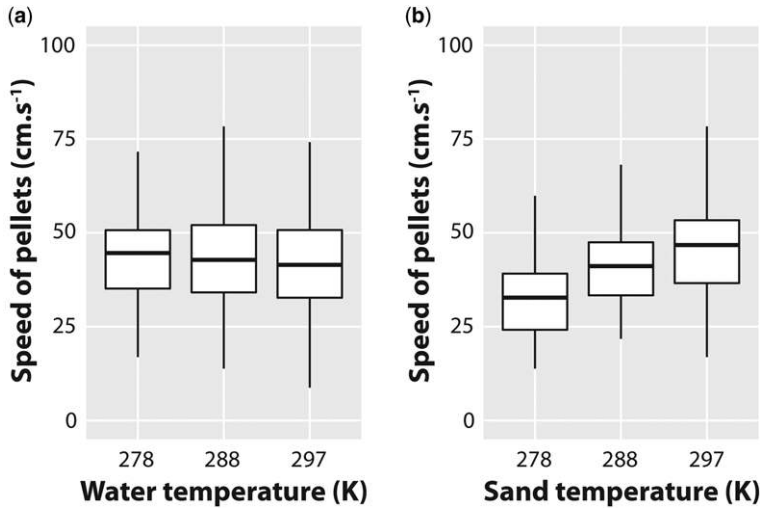
Fig. 16. Speed of pellets v. the sand and water temperatures measured from all experimental runs. The horizontal bold black lines correspond to the median value of the speed, the lower and upper horizontal black lines of the white box correspond to the first quartile and to the third quartile of the data, respectively, and the lower and upper extremities of the vertical black lines correspond to the minimum and maximum speed values, respectively. (**a**) Water temperature. Number of measurements: $T_w = 278$ K: 64; $T_w = 288$ K: 44; $T_w = 297$ K: 85. (**b**) Sand temperature. Number of measurements: $T_s = 278$ K: 26; $T_s = 288$ K: 59; $T_s = 297$ K: 108.

in a transported volume of sediment 9 times larger for experiments at temperatures of 297 K as opposed to those at 278 K (Fig. 13b and Table 3). This result attests to the crucial role of boiling in the transportation processes compared with 'classic' liquid water transport at the surface of Mars.

For all of the experiments we observed that the water was boiling. The fact that the intensity of boiling-related processes (ejection, pellets and avalanches) increases more markedly with sand temperature than water temperature leads us to hypothesize that this factor controls the boiling intensity. At any given pressure above the triple point, boiling can occur when the temperature of water and/or the temperature of the surface in contact with liquid water T_0 exceeds the saturation temperature T_e (a.k.a. 'excess temperature' $\Delta T_{excess} = T_0 - T_e > 0$ K). The saturation temperature changes with atmospheric pressure
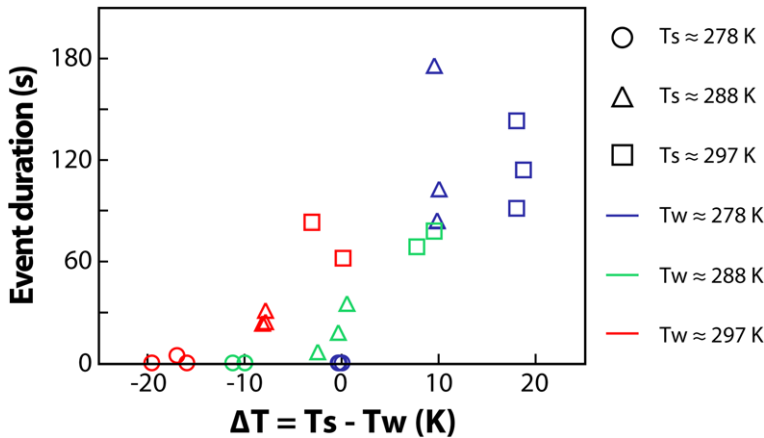

Fig. 17. Plot of the duration of the sand ejection process against the temperature difference, ΔT, between the sand, T_s, and the water, T_w.

(Wagner *et al.* 2011) and in our case the surface temperature corresponds to sand temperature ($T_0 = T_s$). As the pressure inside the chamber is similar between all the experiments, the boiling regime differences depend only on the sand temperature (Cengel & Ghajar 2014; Liang & Mudawar 2017). For our nominal pressure (P_0 *c.* 7 mbar) and sand temperatures ($T_s \geq 278$ K), the liquid water introduced into the MSC is unstable and boils in all of our experiments, because T_e *c.* 275 K (Wagner *et al.* 2011) and therefore $\Delta T_{excess} \geq 3$ K. At sand temperatures greater than 288 K ($\Delta T_{excess} \approx \geq 13$ K), water vapour production is so rapid that we observe entrainment of the sand grains and lifting of millimetre- to centimetre-sized pellets (Fig. 5). If the temperature of the sand is close to or below the frozen point, i.e. if the temperature of excess is negative, the boiling liquid water flow will mainly transport sediment by overland flow similarly to terrestrial water flow and without formation of sand pellets, sand ejection and avalanches (Conway *et al.* 2011; Jouannic *et al.* 2015).

Our observations indicate that water temperature has a minor effect on the intensity of boiling. One might expect the water temperature to be important as the difference in temperature between the liquid and sediment ΔT is known to drive boiling in phreomagmatic eruptions and geysers (Lorenz 2002). We hypothesize that, for any given site of intense boiling, the temperature of the water involved will be reduced to and held at the saturation temperature owing to the latent heat of the phase change, irrespective of its initial temperature.

The excess temperature, ΔT (T_s–T_w), does however influence the duration of sand ejection (Fig. 17). This could be because at nominal pressure the water released is warmer, T_w, than the saturation temperature, T_e, and so the water vaporizes, consuming latent heat and decreasing its temperature to the boiling point. As the vapour is produced, the amount of available water flowing at the surface and percolating into the sand is reduced. The higher the temperature of the water is compared with the boiling point, the more vapour needs to be produced to reach the boiling point, so the more liquid is lost. This hypothesis is supported by the fact that the average relative humidity of the experiments increases with water temperature from 21% at $T_w = 278$ K to 30% at $T_w = 298$ K (Table 3). As sand ejection depends on the contact between the saturated sediment and the dry sediment, a reduction in the water volume results in a reduction in ejection. This is combined with the fact that warmer sand temperature provides the energy required to the phase change and favours the process of sand ejection, as discussed in the section 'Sand grain ejection', because the warm sand provides the additional energy required to perform the phase change. Therefore a large ΔT favours

a longer duration of sand ejection because (1) a colder water temperature favours percolation and (2) a warmer sand temperature provokes more sand ejection. The same logic applies to the duration of the dry sand avalanches (Fig. 5).

This hypothesis is also consistent with the longer length of the overland flow feature measured for cold water temperature. We think that the larger volume of water available at the surface at $T_w = 278$ K induced a slight increase of the flow speed that deposit the sand farther than at higher water temperature (Figs 14 & 15, section 'Overland flow feature').

Massé *et al.* (2016) also reported that boiling water can trigger dry sand avalanches. The temperature of the sand in their experiments was between 288 and 297 K, and the temperature of water was close to the triple point. These conditions are close to those in our experiments which result in instabilities persisting up to tens of seconds after the end of water release (Fig. 5). In contrast, Massé *et al.* (2016) did not observe any persistence. As the main difference between the two series of experiments is the water flow rate (*c.* 11 ml s^{-1} in our work v. *c.* 1–5 ml s^{-1} in Massé *et al.* (2016)), we infer that the amount of liquid water available is the explanation for this difference in persistence. At a low flow rate the propagation of fluid through the sediment never results in supersaturation, which we infer is occurring in our experiments.

Sediment transport mechanisms by boiling water

Sand grain ejection. When unstable liquid water percolates downslope, the liquid water turns into gas inside the grain bed at the boundary between wet sand and dry sand. Under the pressure conditions of the experiment, this can cause the ejection of dry grains locally at the front of the flow. This ejection is possible only under two conditions: (1) if the pressure related to the phase change, referred to as saturation vapour pressure, at the front of the flow is greater than the atmospheric pressure in the chamber; and (2) if the grains are easily detachable from the bed (which is not the case when grains are wet for example).

As we have observed in our experiments, the two parameters which seem to control this phenomenon are (1) the temperature of the dry bed which determines the saturation vapour pressure and determines whether ejection occurs (Fig. 5) and (2) the temperature of the water that seems to influence the duration of the ejection (Fig. 17). For ejection of a particle to occur, the force exerted on the particle by the release of the gas has to overcome the weight of the particle. As a consequence, the velocity of the gas U_g must be greater than the threshold transport velocity to

entrain the particle denoted by U_t. This threshold transport velocity can be estimated from the particle Reynolds number Re_p (equation 1), defined using the dynamic viscosity μ_v, the density of the gas ρ and the modal diameter of the grains D_{50}:

$$Re_p = \frac{\rho \, D_{50} \, U_t}{\mu_v} \qquad (1)$$

The density of the water vapour is evaluated for each experiment with the ideal gas law, evaluated at the sand temperature and at the saturated vapour pressure (on average $\rho = 1.4 \times 10^{-2}$ kg m^{-3}, Table 3). The viscosity is taken at $\mu_v = 1.0 \times 10^{-5}$ kg m^{-1} s^{-1} and $D_{50} = 2.3 \times 10^{-4}$ m. The mean threshold transport velocity value for the particles is $U_t \approx 6$ m s^{-1} (Table 3) for all of the experiments with a mean $Re_p \approx 2$. The threshold value varies slightly depending on the temperature of the sand (Table 3): the hotter the sand, the lower the value ($U_t = 5.7$ m s^{-1} for $T_s \approx 297$ K), which means that particles within the hot sand will be easier to set in motion than those in the cold sand, for which the threshold of transport velocity is slightly greater ($U_t = 6.3$ m s^{-1} for $T_s \approx 278$ K).

We observed that no particles were ejected for almost all runs with cold sand (Fig. 5). If there is no ejection, this implies that the gas velocity U_g is lower than the threshold transport velocity $U_g < U_t$. This gas velocity can be evaluated by the relationship given in Massé *et al.* (2016) (equation 2) where they used a similar experimental configuration:

$$U_g = \frac{R_{eq}^2 \, \Delta P}{8 \, L \, \mu_v} \qquad (2)$$

where μ_v is the dynamic viscosity of the gas, L is the path length through the sand surface layer with an equivalent radius R_{eq} and $\Delta P = P_{sat} - P_0$ is the difference between the saturated vapour pressure P_{sat} and the chamber atmospheric pressure P_0. Using Antoine's equation, we can estimate the saturated vapour pressure P_{sat} (Pa) using the temperature of the sand T_s (equation 3):

$$\text{Log}_{10}\left(\frac{P_{sat}}{P_{ref}}\right) = A - \frac{B}{T_s + C} \qquad (3)$$

with, P_{ref} the standard pressure (1.0×10^5 Pa), T_s the temperature of the sand (K) and A, B and C Antoine's coefficients. For a temperature between 273 and 303 K, corresponding to our experiments, we used an online tool to calculate the following coefficients (http://ddbonline.ddbst.com/Antoine Calculation/AntoineCalculationCGI.exe?compo): $A = 5.40\,221$, $B = 1\,838.675$ and $C = -31.737$ (Yaws

2015). For our experiments $R_{eq} = 7 \times 10^{-5}$ m, $L = 2D_{50}, \mu_v = 1 \times 10^{-5}$ kg m^{-3} and using the mean threshold gas velocity $U_{gmin} = 6$ m s^{-1}, we get a $\Delta P_{min} \approx$ 50 Pa. This is the minimum differential pressure required in all of the experiments to produce ejection.

When the sand is cold, the differential pressure is either not sufficient to allow the ejection of the grains ($\Delta P < 50$ Pa) or it can sometimes reach value above ΔP_{min} with calculated gas velocity up to $U_g = 18$ m s^{-1} (Table 3), allowing potential grain ejection. For warmer sand temperatures, we find a gas velocity between 60 and 90 m s^{-1} for T_s *c.* 288 K and between 220 and 320 m s^{-1} for T_s *c.* 297 K, allowing the ejection of sand grains. Water temperature seems to have no influence on gas velocity (Table 3).

Since we assume that all of the kinetic energy of the gas is transferred to the particle movement, we can therefore calculate the initial velocity of ejection U_e of the particle from our estimated gas velocity U_g. For cold sand temperature, in the case where gas velocity can exceed the threshold velocity, the ejection velocity remains very low ($U_e < 0.03$ m s^{-1}, Table 3). Therefore these calculations confirm that the ejection of grain is not impossible at $T_s \approx$ 278 K but very limited, as observed in the experiments (Fig. 5). At warmer temperature the ejection velocity is greater than 0.18 m s^{-1}. For example, for run S297-W278-1 we estimate the gas velocity to be 227 m s^{-1} and hence the corresponding particle ejection velocity is 0.66 m s^{-1} (Table 3). For this run only, we had the opportunity to take a high-speed video recording at 1000 fps. Using that footage we were able to track some of the particle trajectories using the open source Tracker software version 4.96 (Douglas Brown http://www.opensourcephy sics.org).

In Figure 18, the points obtained from the video are superposed on the model of the ballistic particle trajectory calculated as for Massé *et al.* (2016). We performed our analysis on six particle trajectories. The ejection angle is not the same for all trajectories because there is a randomizing effect introduced by the path taken by the gas between the (shifting) particles, but for any given set of initial conditions we expect the ejection velocity to be of the same order of magnitude (independent of the ejection angle). For this run, we find an average ejection velocity of 0.62 m s^{-1}, which is in good agreement with our theoretical calculations above, which give $U_e = 0.66$ m s^{-1}. This experimental corroboration of our theoretical model, although limited to one run, provides confidence in the validity of our theoretical framework and therefore we can more confidently extrapolate our experimental results to Mars (see the section 'Gravity').

The speeds are consistent with the ones obtained by Massé *et al.* (2016) for temperatures between 288 and 293 K ($U_e \approx 0.35$ m s^{-1} for a tray angle of 30°).
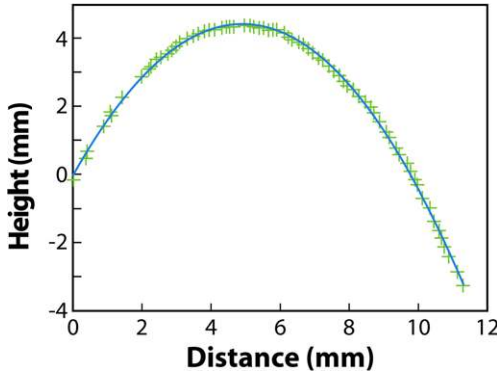
Fig. 18. Example of a trajectory of a sand grain particle extracted from the high-speed video for run S297W297-3. The green crosses are the points used for the ballistic fit (fitted curve in blue).

The authors also observed sand ejection provoked by boiling water which then triggered dry sand avalanches, similar to our observations. However, in their experiments, the saltation produced millimetre-high ridges of sand at the flow front that we did not observe in our experiments. The higher water flow rate in our experiments would have erased such ridges even if they had formed.

Pellet lifting by gas production. Pellets can slide over the sand surface having a reduced contact with the test bed. We hypothesize that pellet levitation is made possible by the lift provided by rapid gas production at the base of the pellet via boiling (Raack et al. 2017). This is a similar physical process to that described as the Leidenfrost effect (Cengel & Ghajar 2014; Liang & Mudawar 2017), but our case differs from the classic effect because instead of a water droplet we have a mixture of a fluid and sand and instead of a solid surface we have a granular bed.

In our experiments the temperature of the surface, T_0 (K), exceeds the saturation temperature, T_{sat} (K), therefore boiling occurs. The surface temperature of the wet sand pellet is maintained at the saturation temperature, T_{sat}, for the fixed pressure inside the chamber. Among the forces that are involved (Raack et al. 2017), the two main competing forces that act on a block lying on a sand bed are: (1) the weight W of the object (equation 4):

$$W = g\rho_{ws}\,HA, \qquad (4)$$

where g is the gravity (m s^{-2}), ρ_{ws} is the density of the wet sand (kg m^{-3}), H is the height of the object (m) and A is the area of the object in contact with the

surface (m^2), and, (2) the lift force F_e (equation 5):

$$F_e = C_f A\,\frac{0.5D\,u_0\,v}{k}\,(\text{from Diniega } et\ al.\ 2013), \qquad (5)$$

where C_f is a geometric coefficient (see Raack et al. 2017 for details), D is the diametre of the area A (m), u_0 is the speed of the ejected gas at the bottom, v is the gas viscosity (Pa s) and k is the sediment permeability (m^2).

On a slope of θ, the movement of the object will occur when the evaporation force F_e caused by the escaping gas exceeds the weight $W\cos\theta$ of the pellet (equation 6):

$$F_e > W\cos\theta \qquad (6)$$

The formation of a cushion of gas means we can neglect the friction force between the surface of the test bed and the pellet (Raack et al. 2017). The water vapour is produced uniformly at the base of the object and perpendicular to the surface with a speed u_0 (m s^{-1}) (equation 7):

$$u_0 = \frac{q}{E_v\,\rho_g} \qquad (7)$$

where q (W m^{-2}) is the heat flux by thermal conduction, E_v is the enthalpy of evaporation for water (J kg^{-1}) and ρ_g is the volatile gas density (kg m^{-3}).

The evaporation rate is constrained by the conductive heat flux from the hot surface to the wet sand pellet. We assume that all of the heat flux is consumed by the phase change. The heat flux (equation 8) is obtained by integrating the solution of the heat equation (Turcotte & Schubert 2002):

$$q(t) = \Delta T_{excess}\,\sqrt{\frac{\lambda C_p \rho_s}{\pi t}}, \qquad (8)$$

where ΔT_{excess} corresponds to the excess temperature ($\Delta T_{excess} = T_0 - T_{sat}$, K), λ is the thermal conductivity of the sand (W m^{-1} K^{-1}), C_p is the heat capacity of the sand (J kg^{-1} K^{-1}), ρ_s is the sand density (kg m^{-3}) and t is the time (s).

The values of the parameters used are presented in Raack et al. (2017), as well as figures presenting the results of the scaling.

In our experiments, the magnitude of the heat flux and therefore the gas production and the lifting force will vary with the excess temperature (equation 8). We observe for the same saturation temperature, T_{sat}, the higher the surface temperature is, the more likely sliding is to occur (Supplementary videos 1, 2, 3, 5 and 7). The heat flux is increased by 4.6 between surface temperatures of 273 and 297 K

(Raack *et al.* 2017). For a similar size and form of object, the sliding duration calculated increases by several tens of seconds. At 278 K we observe limited production of small-sized pellets while at $T_s = 297$ K we observe greater numbers of large-sized pellets with the lifting of the pellets and sliding over the surface with reduced surface friction. The capacity for pellets to slide may be giving us insight into the different boiling regimes being experienced with changes in excess temperature (Cengel & Ghajar 2014; Giraud *et al.* 2015; Liang & Mudawar 2017). We think that experiments at sand temperatures of 278 K ($\Delta T_{excess} \approx 3$ K) are experiencing a different boiling regime, probably a nucleate boiling regime, compared with those at temperature of 297 K ($\Delta T_{excess} \approx 22$ K) for which the behaviour appears to be closer to a film boiling regime with the related Leidenfrost effect (Cengel & Ghajar 2014; Liang & Mudawar 2017). Experiments at the intermediate sand temperature of 288 K ($\Delta T_{excess} \approx 13$ K) may be transitional.

At $T_s = 297$ K, as the gas flux is higher, the size of pellets that could potentially be lifted is larger, up to centimetres in size (Fig. 10a). The larger pellets generally have a flatter shape than the smaller ones that tend to be more spherical (Figs 6a & 10a). The aspect ratio, H/D, of the pellets is a key parameter for levitation. The larger the diameter D (and so the basal area A) of the pellet in contact with the surface is compared with the height H, the smaller the aspect ratio, and hence a larger amount of gas is produced and the lift force is increased with respect to the weight force (equations 4 & 5 and Fig. 19). Scaling of the lift for different aspect ratios at $T_s = 297$ K is presented in Figure 19 and shows that, as the
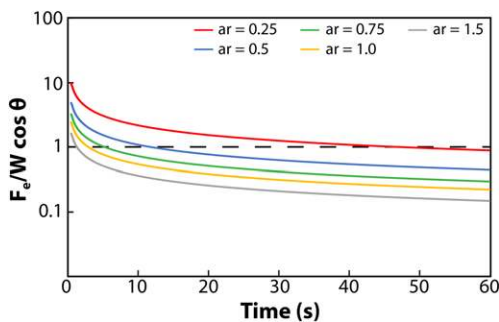

Fig. 19. Evolution of the ratio of the lifting force F_e to the weight force $W \cos \theta$ of a block over a slope of 25°. The ratio is calculated for different aspect ratios (ar) D/H of pellets for a surface temperature of $T_0 = 297$ K and $D = 2$ cm in the Mars Simulation Chamber. The physical parameters of our experiments in the Mars Simulation Chamber can be found in Raack *et al.* (2017). Levitation occurs when the ratio $F_e/W \cos \theta$ is greater than 1 (dashed black line).

aspect ratio increases to 1 (more spherical), levitation of pellets becomes less likely compared with flattened pellets.

The variation in shape of the pellets seems to be linked to their formation process. They form when the boiling water interacts with the sand surface. The water percolates into the sand, but owing to its instability, the liquid changes into gas permitting the detachment of these wet sand pellets. At the lower surface temperature tested, the heat flux is enough to lift up spherical millimetre-sized pellets (Supplementary videos 1 (left), 2 (left), 5 (left) and 6). These small pellets either detach from the edge of the saturated area or are directly formed on the initial contact between the water and the sand. At higher temperatures, we still observe the formation of these small pellets, but also larger flattened ones (Supplementary videos 1 (right), 2 (right), 5 (right), 7 and 8). For the flattened pellets, there is a complex interplay between the liquid flow rate, the percolation and the heat flux which result in their formation. When the liquid flows over the surface it also percolates into the sand. When the basal surface area (the saturated area) becomes large enough to support the weight of the object, detachment of the pellet from the source area can occur. This is nicely illustrated at 11 s into Supplementary video 8 where a centimetre-sized pellet detaches from the saturated area, but only once its surface area reaches a threshold size.

The observation that pellet production reduces sharply after the first few seconds of the water release could be explained by the rate of overland flow and percolation overwhelming the lifting by wetting a sufficient sand area to reduce the production of large pellets. This same explanation can be used to explain why formation of the overland flow feature is delayed by about 20 s for experiments performed at $T_s = 297$ K compared with the others. The more intense gas production allows larger masses of saturated sand at the source area to be transported downslope in pellet form, retarding the formation of the saturated zone. We notice also that the flow rate must play a role in the formation of pellets as at lower flow rate (c. 1–5 ml s^{-1}) but similar temperature/atmospheric conditions with a similar sand; this process was not observed (Massé *et al.* 2016).

In addition, our simple conceptual model of pellet levitation predicts that pellets should move faster at higher surface temperatures, as observed in our experiments (Fig. 16b), because a higher lift force results in a reduced surface friction (equations 5, 7 & 8).

Implication for Martian landscape studies

Gravity. Martian gravity, about one-third of terrestrial gravity, can modify boiling regimes (Cengel & Ghajar 2014) and therefore is likely to influence

the size of features and the propagation speeds of objects set into motion by boiling. Scaling calculations predict that the process of sand ejection should result in about three times more sediment transport under Martian gravity compared with terrestrial gravity (Massé *et al.* 2016). A similar approach to Massé *et al.* (2016) is presented here to examine the influence of gravity on the entrainment of grains for our experimental characteristics (see the section 'Sand grain ejection'). We consider the same geometric, pressure and temperature configurations as our experiments, but change the gravitational acceleration from 9.8 to 3.7 m s^{-2}. The lower Martian gravity decreases the transport threshold velocity, U_t, to around 2.5 m s^{-1}, resulting in a lower ΔP_{min} of *c.* 20 Pa. This value is lower than the 50 Pa value calculated for terrestrial gravity (see the section 'Sand grain ejection'), but nevertheless even this reduced value would not result in ejection for sand at T_s = 278 K, since the gas velocity U_g is still <2.5 m s^{-1} and too small for ejection. Considering that the atmospheric pressure, dynamic viscosity of the gas and path length through the sand surface layer with an equivalent radius should be the same on Mars, the ejection velocity for Mars should be similar to that in our experiments, as discussed in more detail in Massé *et al.* (2016). The ballistic trajectory of the particle will be influenced by the change of gravity: for a given ejection angle, the ratio of the height to the length of a trajectory would be 2.6 times greater on Mars than on Earth.

Reduced gravitational acceleration also favours the lifting of objects through gas production by phase change (Diniega *et al.* 2013; Raack *et al.* 2017). The weight (equation 4) is directly related to gravity and so a reduction of gravity decreases the weight force. As a result the object is more easily lifted. From scaling calculations, Raack *et al.* (2017) conclude that the lifting process under weaker Martian gravity is enhanced by about a factor of 7, is able to transport larger objects for a longer time and should continue be an efficient process, even at temperatures close to the saturation point. Therefore an increase in the process of pellet production should also increase the area affected by the transport of sediment and the amount of transported volume under Martian gravity compared with our experiments on Earth. Even if the pellet speed may be one-third slower on Mars as it is driven by gravity, it is counteracted by the fact that the sliding duration should be longer, so the downslope spatial extent of the features associated with pellets may approach decametres in size and so should be visible, but not identifiable, using remote sensing data (Raack *et al.* 2017).

Martian gullies. Our experimental results have potential implications for the formation and current activity of gullies on Mars. If liquid water can reach the surface then it is likely that the water will boil (see the section 'Stability of liquid water at the surface of Mars'), but owing to the scale of our experiments the morphologies observed are not directly comparable with the morphology of Martian gullies. In addition, we have not directly attempted to incorporate the effect of reduced Martian gravity in our experiments. However, the surface temperatures and pressures simulated in our experiments are realistic for Mars (section 'Gullies on Mars') and could occur at sites where gullies are found. Therefore, our experiments reveal sediment transport processes that could occur in gullies if liquid water is indeed involved. Our calculations reveal that these boiling-related sediment transport processes should be amplified compared with those observed in our experiments owing to the lower Martian gravity (see the section 'Gravity'). In this section, we discuss how our experimental results could influence future estimates of the water budget of Martian gullies (taking into account the caveats of flowrate and water source), and speculate on the implications of our results for brines and for processes contributing to gully formation in the past.

Experiments and physical analyses have shown that the unusual physical processes directly associated with boiling (sand saltation, pellet lifting, avalanches) significantly enhance the amount of sediment transported compared with stable liquid water flow (Massé *et al.* 2016; Raack *et al.* 2017; this study), and in addition produce distinct morphological features. This means that the amount of water required to produce changes in gullies may have been overestimated so far (Heldman *et al.* 2005; Pelletier *et al.* 2008; Parsons & Nimmo 2010) and these changes should be observable at the resolution of orbital instruments (Raack *et al.* 2017). Although the sediment transport should be visible, current imaging techniques do not allow us to uniquely identify boiling as the primary transport process – current datasets have not even allowed us to convincingly distinguish, based on flow-morphology alone, between CO_2-gas-supported or water-rich debris flow as the sediment transporting fluid. As outlined in the introductory section, one of the challenges for the water hypothesis is the perceived paucity of the possible reservoirs compared with the high frequency and volume of the landform. Our results somewhat alleviate this problem and maintain liquid water as a strong candidate to explain the formation of gullies in the past and their ongoing evolution. The potential effects of boiling cannot be overlooked in future studies of liquid water explaining current or past activity in gullies.

In our experiments we used a relative stable flow rate (*c.* 11 ml s^{-1}), which is many times smaller than flow rates estimated for Martian gullies (Heldmann

et al. 2005; Mangold *et al.* 2010; Parsons & Nimmo 2010; Goldspiel & Squyres 2011; Jouannic *et al.* 2012). Comparison between our work and previous experiments has highlighted the importance of the flow rate in the physics of sediment transport and resulting morphology (Massé *et al.* 2016). This is an area that warrants future investigation, although similar processes were observed in unpublished experiments run at 40–50 ml s^{-1} (Conway, pers. comm.), hence we predict similar processes to continue even at higher flow rates more applicable to Martian gullies.

We did not attempt to faithfully recreate the source of the water for Martian gullies, which could be a topic of future experiments; however, we did test a range of water temperatures relevant to the proposed water sources. If the water originates directly from the melting of ice, then the initial water temperature will be close to the fusion point. So the most relevant cases are our experiments performed with the coldest water temperature ($T_w = 278$ K) or the experiments performed by Massé *et al.* (2016) depending on the flow rate considered. If the water originated from a perched reservoir or an aquifer then it could potentially be warmer, and in that case all the temperature combinations in our experiments could be relevant.

Salts are thought to be common at the Martian surface from theoretical considerations (Gooding 1978) and orbital and rover observations (e.g. Squyres *et al.* 2004; Hecht *et al.* 2009; Carter *et al.* 2013). In addition, recent spectroscopic detection of hydrated minerals supports the potential for briny flows at the surface of Mars (Ojha *et al.* 2015). Brines could therefore be involved in the evolution of gullies (Chevrier *et al.* 2009; McEwen *et al.* 2014) but the origin of the water/brines is unknown and still under debate. Even though we did not perform our experiments with brine compositions, we argue that it is also likely that similar boiling-induced transport mechanisms could occur, for the following reasons. At a given pressure, the presence of salt will increase the boiling temperature, whose magnitude is dependent on the nature of the salt and its concentration in the solution (Atkins & de Paula 2006; Masterton & Hurley 2011). Taking as an example an eutectic brine solution of $MgSO_4$ (25 wt%), the boiling temperature will be 2 K higher than for pure liquid water (Masterton & Hurley 2011). Considering that the temperature at the Martian surface can exceed 285 K (Haberle *et al.* 2001; Reiss & Jaumann 2003; Fenton 2006; McEwen *et al.* 2014; Martín-Torres *et al.* 2015), boiling is still possible with such brines. Previous experiments at low pressure have shown that both brines and liquid water experience boiling-related sediment transport, although for the brines the expression of the resulting surface morphologies is reduced (Massé *et al.* 2016).

Classical gullies have been dated to be no older than several million years (during the late Amazonian period; Reiss *et al.* 2004; Schon *et al.* 2009; Raack *et al.* 2012). During this period, the atmospheric conditions are thought to be generically similar to the ones observed today – low pressure, dry and cold (Marchant & Head 2007), inhibiting the production of abundant liquid water at the surface. However, increases in orbital obliquity up to 35° have occurred during the last 5 Ma, which can result in non-negligible changes in climatic conditions (Laskar *et al.* 2002, 2004) and in an increased potential for transient liquid water (Richardson & Mischna 2005). Primarily these changes are brought about by increased sublimation of the polar caps (which receive more insolation at higher obliquity), increasing the overall atmospheric pressure and humidity (Madeleine *et al.* 2014). This effect could be further enhanced by release of the CO_2 currently trapped within the south polar cap, which could increase the atmospheric density by 4–5 mbar, which could have happened as recently as 600 ka (Phillips *et al.* 2011). Such atmospheric pressures would not be enough to make water stable but increase the spatial and temporal extent of transient liquid water. Therefore boiling may also have been involved in the formation of gullies in the past.

Other Martian surface features. Beside gullies, remote sensing data reveal a diversity of slope morphologies associated with different active mass wasting processes at the surface of Mars. Our experimental results could have implications for the numerous flow-like features that appear very recent and still active today, including:

(1) Recurring Slope Lineae (RSL; McEwen *et al.* 2011, 2014; Ojha *et al.* 2014, 2015; Stillman *et al.* 2014, 2016, 2017; Chojnacki *et al.* 2016), which are narrow (0.5–5 m) and several hundred metres long. Each year they incrementally grow for several weeks during the warm season, fade and then reappear the next year (McEwen *et al.* 2011; Ojha *et al.* 2014). The leading proposed mechanism is that their formation is triggered by briny flows (McEwen *et al.* 2011, 2014; Chevrier & Rivera-Valentin 2012; Ojha *et al.* 2014, 2015, Grimm *et al.* 2014; Chojnacki *et al.* 2016; Stillman *et al.* 2014, 2016, 2017). Such brines are expected to boil at RSL conditions (Massé *et al.* 2016). At 7 mbar the boiling temperature for a brine solution ($MgSO_4$ 25% wt) is expected *c.* 277 K. The sites of active RSL are characterized by their relatively high surface temperatures that can reach 300 K (McEwen *et al.* 2014). Therefore, the excess temperature should be sufficient to allow boiling of the brine and potentially reach a Liedenfrost-like

regime. According to these surface temperatures and depending on the concentration and salts involved, a similar behaviour is expected for the brines as observed in our pure water experiments for slightly higher surface temperatures.

(2) Dark dune flows (Fenton *et al.* 2003; Kieffer *et al.* 2006; Horvath *et al.* 2009; Kereszturi *et al.* 2009; Gardin *et al.* 2010, Möhlmann & Kereszturi 2010; Hansen *et al.* 2011, 2013) are several tens of metres long and metres wide emanating from Dark Dune Spots and they form during local spring at low temperatures (150–180 K; Kereszturi *et al.* 2010) The leading hypothesis for the dark flows is that the material deposited in the dark spots is remobilized by ongoing sublimation of CO_2 slab ice (Gardin *et al.* 2010). An alternative hypothesis is that these dark flows are caused by viscous liquid film flow (Horvath *et al.* 2009; Möhlmann & Kereszturi 2010; Kereszturi *et al.* 2010). This flow involves the formation of an interfacial water film on the sand grains and the presence of brines to decrease the eutectic point (down to 245 K). The possibility of boiling is not discussed, but for salty solutions boiling would occur at warmer temperatures than for pure water (Masterton & Hurley 2011). At spring temperatures the water is unlikely to boil, but it cannot be excluded if the P/T are close to the triple point.

(3) Slope streaks (Morris 1982; Ferguson & Lucchitta 1984; Sullivan *et al.* 2001, Malin & Edgett 2001; Schorghofer *et al.* 2007; Chuang *et al.* 2007, Bergonio *et al.* 2013; Brusnikin *et al.* 2016) are several hundreds of metres to kilometres long and develop on steep slopes, following the topographic gradient. Multitemporal observations have revealed their present-day activity (Malin & Edgett 2001; Sullivan *et al.* 2001; Aharonson *et al.* 2003; Brusnikin *et al.* 2016). Several processes have been proposed to explain these features, where most authors prefer dry mechanisms (Sullivan *et al.* 2001; Miyamoto *et al.* 2004; Baratoux *et al.* 2006; Chuang *et al.* 2007), including the influence of diurnal CO_2 sublimation (Piqueux *et al.* 2016). However, some of the morphological attributes are hard to explain with dry flows (Brusnikin *et al.* 2016) and therefore wet mechanisms cannot be excluded and these may involve brine solutions (Ferguson & Lucchitta 1984; Ferris *et al.* 2002; Miyamoto *et al.* 2004; Marchant & Head 2007; Kreslavsky & Head 2009; Mushkin *et al.* 2010; Kolb *et al.* 2010). If liquid water is present in these features then the boiling mechanisms presented here should be possible because they form at low latitudes and on high slopes where the surface temperatures can be locally high (McEwen *et al.* 2014).

Conclusions

Our experiments highlight boiling as an important agent of sediment transport, which should not be neglected when analysing and modelling flow features on Mars for which water is a candidate fluid. In the context of this special issue we particularly draw attention to the fact that, if liquid water is present, boiling could be important in understanding recent changes in Martian gullies, but also for gully modifications under high-obliquity conditions in the past. We find that sediment transport by boiling is characterized by grain ejection, granular avalanches and levitating pellets, which according to our scaling calculations are all more effective transport processes under Martian gravity. Only a small amount of water is required to mobilize a relatively large volume of sediment over long distances.

Among the two parameters investigated in our experiments – the water and sand temperatures – it appears that the sand temperature is the main controlling parameter of the transport via boiling. Therefore this mechanism would be favoured where high surface temperatures are experienced on Mars (e.g. equatorial RSL at the present day). The difference in the balance between the observed physical processes and their resultant morphologies arises from different intensities of boiling – which is controlled primarily by atmospheric pressure (boiling temperature) and the surface temperature (sand temperature) – hence in our experiments boiling transitions from a regime similar to nucleate boiling to a regime similar to film boiling associated with the Leidenfrost effect.

We found that water temperature plays a minor role in this transition, but does have some control over the runout length of the overland flow and the duration of the grain ejection and dry avalanche processes by influencing the amount of liquid water available.

Further experimental work and numerical modelling need to be done to explore the range of parameters, such as grain size of the sediments and flow rate of the water, to further constrain the potential geomorphological role of the boiling water on planetary surfaces. Our results and the potential influence of the boiling of water should also be considered for other active landforms on Mars, including recurring slope lineae, dark dune flows and slope streaks that potentially involve liquid water.

References

AHARONSON, O., SCHORGHOFER, N. & GERSTELL, M.F. 2003. Slope streak formation and dust deposition rates on Mars. *Journal of Geophysical Research – Planets*, **108**, 5138.

ARFSTROM, J. & HARTMANN, W.K. 2005. Martian flow features, moraine-like ridges, and gullies: terrestrial analogs and interrelationships. *Icarus*, **174**, 321–335.

ATKINS, P. & DE PAULA, J. 2006. *Physical Chemistry*. W. H. Freeman, New York.

ATWOOD-STONE, C. & MCEWEN, A.S. 2013. Avalanche slope angles in low-gravity environments from active Martian sand dunes. *Geophysical Research Letters*, **40**, 2929–2934.

BALME, M.R., MANGOLD, N. *ET AL.* 2006. Orientation and distribution of recent gullies in the southern hemisphere of Mars: observations from High Resolution Stereo Camera/Mars Express (HRSC/MEX) and Mars Orbiter Camera/Mars Global Surveyor (MOC/MGS) data. *Journal of Geophysical Research – Planets*, **111**, E05001.

BARATOUX, D., MANGOLD, N. & THE HRSC CO-INVESTIGATOR TEAM 2006. The role of the wind-transported dust in slope streaks activity: evidence from the HRSC data. *Icarus*, **183**, 30–45.

BERGONIO, J.R., ROTTAS, K.M. & SCHORGHOFER, N. 2013. Properties of Martian slope streak populations. *Icarus*, **225**, 194–199.

BERMAN, D.C., HARTMANN, W.K., CROWN, D.A. & BAKER, V.R. 2005. The role of arcuate ridges and gullies in the degradation of craters in the Newton Basin region of Mars. *Icarus*, **178**, 465–486.

BRASS, G.W. 1980. Stability of brines on Mars. *Icarus*, **42**, 20–28.

BRIDGES, N.T., SULLIVAN, R. *ET AL.* 2017. Martian aeolian activity at the Bagnold Dunes, Gale Crater: the view from the surface to orbit. *Journal of Geophysical Research – Planets*, **122**, 2077–2110, https://doi.org/10.1002/2017JE005263

BRUSNIKIN, E.S., KRESLAVSKY, M.A., ZUBAREV, A.E., PATRATIY, V.D., KRASILNIKOV, S.S., HEAD, J.W. & KARACHEVTSEVA, I.P. 2016. Topographic measurements of slope streaks on Mars. *Icarus*, **278**, 52–61.

CARTER, J., POULET, F., BIBRING, J.P., MANGOLD, N. & MURCHIE, S. 2013. Hydrous minerals on Mars as seen by the CRISM and OMEGA imaging spectrometers: updated global view. *Journal of Geophysical Research: Planets*, **118**, 831–858.

CEDILLO-FLORES, Y., TREIMAN, A.H., LASUE, J. & CLIFFORD, S.M. 2011. CO_2 gas fluidization in the initiation and formation of Martian polar gullies. *Geophysical Research Letters*, **38**, L21202.

CENGEL, Y.A. & GHAJAR, A.J. 2014. *Heat and Mass Transfer: Fundamentals and Applications*. McGraw-Hill Education, New York.

CHEVRIER, V.F., ULRICH, R. & ALTHEIDE, T.S. 2009. Viscosity of liquid ferric sulfate solutions and application to the formation of gullies on Mars. *Journal of Geophysical Research – Planets*, **114**, E06001.

CHEVRIER, V.F. & RIVERA-VALENTIN, E.G. 2012. Formation of recurring slope lineae by liquid brines on present-day Mars. *Geophysical Research Letters*, **39**, L21202.

CHOJNACKI, M., MCEWEN, A.S., DUNDAS, C., OJHA, L., URSO, A. & SUTTON, S. 2016. Geologic context of recurring slope lineae in Melas and Coprates Chasmata, Mars. *Journal of Geophysical Research*, **121**, 1204–1231.

CHRISTENSEN, P.R. 2003. Formation of recent Martian gullies through melting of extensive water-rich snow deposits. *Nature*, **422**, 45–48.

CHUANG, F.C., BEYER, R.A., MCEWEN, A.S. & THOMSON, B.J. 2007. HiRISE observations of slope streaks on Mars. *Geophysical Research Letters*, **34**, L20204.

CONWAY, S.J. & BALME, M.R. 2016. A novel topographic parameterization scheme indicates that Martian gullies display the signature of liquid water. *Earth and Planetary Science Letters*, **454**, 36–45.

CONWAY, S.J., LAMB, M.P., BALME, M.R., TOWNER, M.C. & MURRAY, J.B. 2011. Enhanced runout and erosion by overland flow at low pressure and sub-freezing conditions: experiments and application to Mars. *Icarus*, **211**, 443–457.

CONWAY, S.J., BALME, M.R., KRESLAVSKY, M.A., MURRAY, J.B. & TOWNER, M.C. 2015. The comparison of topographic long profiles of gullies on Earth to gullies on Mars: a signal of water on Mars. *Icarus*, **253**, 189–204.

CONWAY, S.J., HARRISON, T.N., SOARE, R.J., BRITTON, A.W. & STEELE, L.J. 2018. New slope-normalized global gully density and orientation maps for Mars. *In*: CONWAY, S.J., CARRIVICK, J.L., CARLING, P.A., DE HAAS, T. & HARRISON, T.N. (eds) *Martian Gullies and their Earth Analogues*. Geological Society, London, Special Publications, **467**. First published online November 27, 2017, https://doi.org/10.1144/SP467.3

COSTARD, F., FORGET, F., MANGOLD, N. & PEULVAST, J. 2002. Formation of recent Martian debris flows by melting of near-surface ground ice at high obliquity. *Science*, **295**, 110–113.

DI ACHILLE, G., SILVESTRO, S. & ORI, G.G. 2008. Defrosting processes on dark dunes: new insights from HiRISE images at Noachis and Aonia Terrae, Mars. *In*: *Planetary Dunes Workshop*, 29 April–2 May, Alamogordo, New Mexico, 27–28.

DICKSON, J.L., HEAD, J.W. & KRESLAVSKY, M. 2007. Martian gullies in the southern mid-latitudes of Mars: evidence for climate-controlled formation of young fluvial features based upon local and global topography. *Icarus*, **188**, 315–323.

DINIEGA, S., BYRNE, S., BRIDGES, N.T., DUNDAS, C.M. & MCEWEN, A.S. 2010. Seasonality of present-day Martian dune-gully activity. *Geology*, **38**, 1047–1050.

Diniega, S., Hansen, C.J., McElwaine, J.N., Hugenholtz, C.H., Dundas, C.M., McEwen, A.S. & Bourke, M.C. 2013. A new dry hypothesis for the formation of Martian linear gullies. *Icarus*, **225**, 526–537.

Dundas, C.M., McEwen, A.S., Diniega, S., Byrne, S. & Martinez-Alonso, S. 2010. New and recent gully activity on Mars as seen by HiRISE. *Geophysical Research Letters*, **37**, L07202.

Dundas, C.M., Diniega, S., Hansen, C.J., Byrne, S. & McEwen, A.S. 2012. Seasonal activity and morphological changes in Martian gullies. *Icarus*, **220**, 124–143.

Dundas, C.M., Diniega, S. & McEwen, A.S. 2015. Long-term monitoring of Martian gully formation and evolution with MRO/HiRISE. *Icarus*, **251**, 244–263.

Dundas, C.M., McEwen, A.S., Diniega, S., Hansen, C.J., Byrne, S. & McElwaine, J.N. 2018. The formation of gullies on Mars today. *In*: Conway, S.J., Carrivick, J.L., Carling, P.A., de Haas, T. & Harrison, T.N. (eds) *Martian Gullies and their Earth Analogues*. Geological Society, London, Special Publications, **467**. First published online November 27, 2017, https://doi.org/10.1144/SP467.5

Edgett, K.S. & Christensen, P.R. 1991. The particle size of Martian aeolian dunes. *Journal of Geophysical Research*, **96**, 22,765–22,776.

Fenton, L.K. 2006. Dune migration and slip face advancement in the Rabe Crater dune field, Mars. *Geophysical Research Letters*, **33**, L20201.

Fenton, L.K., Bandfield, J.L. & Ward, A.W. 2003. Aeolian processes in Proctor Crater on Mars: sedimentary history as analyzed from multiple data sets. *Journal of Geophysical Research*, **108**, 5129.

Ferguson, H.M. & Lucchitta, B.K. 1984. Dark streaks on talus slopes, Mars. *NASA Washington Report of Planetary Geology Programs*, 188–190.

Ferris, J.C., Dohm, J.M., Baker, V.R. & Maddock, III, T. 2002. Dark slope streaks on Mars: are aqueous processes involved? *Geophysical Research Letters*, **29**, 1490.

Gaidos, E. 2001. Cryovolcanism and the recent flow of liquid water on Mars. *Icarus*, **153**, 218–223.

Gardin, E., Allemand, P., Quantin, C. & Thollot, P. 2010. Defrosting, dark flow features, and dune activity on Mars: example in Russell crater. *Journal of Geophysical Research – Planets*, **115**, E06016.

Gilmore, M.S. & Phillips, E.L. 2002. Role of aquicludes in formation of Martian gullies. *Geology*, **30**, 1107–1110.

Giraud, F., Rullière, R., Toublanc, C., Clausse, M. & Bonjour, J. 2015. Experimental evidence of a new regime for boiling of water at subatmospheric pressure. *Experimental Thermal and Fluid Science*, **60**, 45–53.

Goldspiel, J.M. & Squyres, S.W. 2011. Groundwater discharge and gully formation on Martian slopes. *Icarus*, **211**, 238–258.

Gooding, J.L. 1978. Chemical weathering on Mars: thermodynamic stabilities of primary minerals (and their alteration products) from mafic igneous rocks. *Icarus*, **33**, 483–513.

Grimm, R.E., Harrison, K.P. & Stillman, D.E. 2014. Water budgets of Martian recurring slope lineae. *Icarus*, **233**, 316–327.

Haberle, R.M., McKay, C.P., Schaeffer, J., Cabrol, N.A., Grin, E.A., Zent, A.P. & Quinn, R. 2001. On the possibility of liquid water on present-day Mars. *Journal of Geophysical Research – Planets*, **106**, 23317–23326.

Hansen, C.J., Bourke, M. *et al.* 2011. Seasonal erosion and restoration of Mars' northern polar dunes. *Science*, **331**, 575–578.

Hansen, C.J., Byrne, S. *et al.* 2013. Observations of the northern seasonal polar cap on Mars I. Spring sublimation activity and processes. *Icarus*, **225**, 881–897.

Harrison, T.N., Osinski, G.R., Tornabene, L.L. & Jones, E. 2015. Global documentation of gullies with the Mars Reconnaissance Orbiter Context Camera and implications for their formation. *Icarus*, **252**, 236–254.

Hartmann, W.K., Thorsteinsson, T. & Sigurdsson, F. 2003. Martian hillside gullies and Icelandic analogs. *Icarus*, **162**, 259–277.

Head, J.W., Marchant, D.R. & Kreslavsky, M.A. 2008. Formation of gullies on Mars: link to recent climate history and insolation microenvironments implicate surface water flow origin. *Proceedings of the National Academy of Sciences of the United States of America*, **105**, 13258–13263.

Hecht, M.H. 2002. Metastability of liquid water on Mars. *Icarus*, **156**, 373–386.

Hecht, M.H., Kounaves, S.P. *et al.* 2009. Detection of perchlorate and the soluble chemistry of Martian soil at the Phoenix lander site. *Science*, **325**, 64–67.

Heldmann, J.L. & Mellon, M.T. 2004. Observations of Martian gullies and constraints on potential formation mechanisms. *Icarus*, **168**, 285–304.

Heldmann, J.L., Toon, O.B., Pollard, W.H., Mellon, M.T., Pitlick, J., McKay, C.P. & Andersen, D.T. 2005. Formation of Martian gullies by the action of liquid water flowing under current Martian environmental conditions. *Journal of Geophysical Research – Planets*, **110**, E05004.

Heldmann, J.L., Carlsson, E., Johansson, H., Mellon, M.T. & Toon, O.B. 2007. Observations of Martian gullies and constraints on potential formation mechanisms II. The northern hemisphere. *Icarus*, **188**, 324–344.

Hess, S.L., Ryan, J.A., Tillman, J.E., Henry, R.M. & Leovy, C.B. 1980. The annual cycle of pressure on Mars measured by Viking Landers 1 and 2. *Geophysical Research Letters*, **7**, 197–200.

Hoffman, N. 2000. Ideas about the surface runoff features on Mars. *Science*, **290**, 711–714.

Hoffman, N. 2002. Active polar gullies on Mars and the role of carbon dioxide. *Astrobiology*, **2**, 313–323.

Horvath, A., Kereszturi, A., Berczi, S., Sik, A., Pocs, T., Ganti, T. & Szathmary, E. 2009. Analysis of Dark Albedo Features on a Southern Polar Dune Field of Mars. *Astrobiology*, **9**, 90–103.

Hourdin, F., Forget, F. & Talagrand, O. 1995. The sensitivity of the Martian surface pressure and atmospheric mass budget to various parameters: a comparison between numerical simulations and Viking observations. *Journal of Geophysical Research*, **100**, 5501–5523.

Hugenholtz, C.H. 2008. Frosted granular flow: a new hypothesis for mass wasting in Martian gullies. *Icarus*, **197**, 65–72.

Ingersoll, A.P. 1970. Mars: occurrence of liquid water. *Science*, **168**, 972–973.

Ishii, T. & Sasaki, S. 2004. Formation of recent Martian gullies by avalanches of CO_2 frost. Abstract 1556

presented at the 35th Lunar and Planetary Science Conference 15–19 March, League City, Texas.

JOHNSON, J.R., ACHILLES, C. *ET AL.* 2017. Visible/near-infrared spectral diversity from in situ observations of the Bagnold Dune Field sands in Gale Crater, Mars. *Journal of Geophysical Research – Planets*, **122**, 2655–2684, https://doi.org/10.1002/2016JE005187

JOUANNIC, G., GARGANI, J., COSTARD, F., ORI, G.G., MARMO, C., SCHMIDT, F. & LUCAS, A. 2012. Morphological and mechanical characterization of gullies in a periglacial environment: the case of the Russell crater dune (Mars). *Planetary and Space Science*, **71**, 38–54.

JOUANNIC, G., GARGANI, J. *ET AL.* 2015. Laboratory simulation of debris flows over sand dunes: insights into gully-formation (Mars). *Geomorphology*, **231**, 101–115.

JOUANNIC, G., GARGANI, J. *ET AL.* In review. Morphological characterization of landforms produced by springtime seasonal activity on Russell dune (Mars). *In*: CONWAY, S.J., CARRIVICK, J.L., CARLING, P.A., DE HAAS, T. & HARRISON, T.N. (eds) *Martian Gullies and Their Earth Analogues*. Geological Society, London, Special Publications, **467**.

KERESZTURI, A., MÖHLMANN, D., BERCZI, S., GANTI, T., KUTI, A., SIK, A. & HORVATH, A. 2009. Recent rheologic processes on dark polar dunes of Mars: driven by interfacial water? *Icarus*, **201**, 492–503.

KERESZTURI, A., MÖHLMANN, D. *ET AL.* 2010. Indications of brine related local seepage phenomena on the northern hemisphere of Mars. *Icarus*, **207**, 149–164.

KIEFFER, H.H., MARTIN, T.Z., PETERFREUND, A.R., JAKOSKY, B.M., MINER, E.D. & PALLUCONI, F.D. 1977. Thermal and albedo mapping of Mars during the Viking primary mission. *Journal of Geophysical Research*, **82**, 4249–4291.

KIEFFER, H.H., CHRISTENSEN, P.R. & TITUS, T.N. 2006. CO_2 jets formed by sublimation beneath translucent slab ice in Mars' seasonal south polar ice cap. *Nature*, **442**, 793–796.

KLEINHANS, M.G., MARKIES, H., DE VET, S.J., VELD, A.C.I. & POSTEMA, F.N. 2011. Static and dynamic angles of repose in loose granular materials under reduced gravity. *Journal of Geophysical Research*, **116**, E11004.

KNEISSL, T., REISS, D., VAN GASSELT, S. & NEUKUM, G. 2010. Distribution and orientation of northern-hemisphere gullies on Mars from the evaluation of HRSC and MOC-NA data. *Earth and Planetary Science Letters*, **294**, 357–367.

KOLB, K.J., PELLETIER, J.D. & MCEWEN, A.S. 2010. Modeling the formation of bright slope deposits associated with gullies in Hale Crater, Mars: implications for recent liquid water. *Icarus*, **205**, 113–137.

KOSSACKI, K.J. & MARKIEWICZ, W.J. 2004. Seasonal melting of surface water ice condensing in Martian gullies. *Icarus*, **171**, 272–283.

KRESLAVSKY, M.A. & HEAD, J.W. 2009. Slope streaks on Mars: a new 'wet' mechanism. *Icarus*, **201**, 517–527.

LAPOTRE, M.G.A., EHLMANN, B.L. *ET AL.* 2017. Compositional variations in sands of the Bagnold Dunes, Gale Crater, Mars, from visible-shortwave infrared spectroscopy and comparison with ground truth from the Curiosity Rover. *Journal of Geophysical Research – Planets*, **122**, 2489–2509, https://doi.org/10.1002/2016JE005133

LASKAR, J., LEVRARD, B. & MUSTARD, J.F. 2002. Orbital forcing of the Martian polar layered deposits. *Nature*, **419**, 375–377.

LASKAR, J., CORREIA, A.C.M., GASTINEAU, M., JOUTEL, F., LEVRARD, B.P. & ROBUTEL. 2004. Long term evolution and chaotic diffusion of the insolation quantities of Mars. *Icarus*, **170**, 343–364.

LIANG, G. & MUDAWAR, I. 2017. Review of drop impact on heated walls. *International Journal of Heat and Mass Transfer*, **106**, 103–126.

LOBITZ, B., WOOD, B.L., AVERNER, M.M. & MCKAY, C.P. 2001. Use of spacecraft data to derive regions on Mars where liquid water would be stable. *Proceedings of the National Academy of Sciences of the United States of America*, **98**, 2132–2137.

LORENZ, R. 2002. Thermodynamics of Geysers: application to Titan. *Icarus*, **156**, 176–183.

MADELEINE, J.B., HEAD, J.W. *ET AL.* 2014. Recent ice ages on Mars: the role of radiatively active clouds and cloud microphysics. *Geophysical Research Letters*, **41**, 4873–4879.

MALIN, M.C. & EDGETT, K.S. 2000. Evidence for recent groundwater seepage and surface runoff on Mars. *Science*, **288**, 2330–2335.

MALIN, M.C. & EDGETT, K.S. 2001. Mars Global Surveyor Mars Orbiter Camera: interplanetary cruise through primary mission. *Journal of Geophysical Research – Planets*, **106**, 23429–23570.

MALIN, M.C., EDGETT, K.S., POSIOLOVA, L.V., MCCOLLEY, S.M. & DOBREA, E.Z.N. 2006. Present-day impact cratering rate and contemporary gully activity on Mars. *Science*, **314**, 1573–1577.

MANGOLD, N., COSTARD, F. & FORGET, F. 2003. Debris flows over sand dunes on Mars: evidence for liquid water. *Journal of Geophysical Research – Planets*, **108**, 5027.

MANGOLD, N., MANGENEY, A., MIGEON, V., ANSAN, V., LUCAS, A., BARATOUX, D. & BOUCHUT, F. 2010. Sinuous gullies on Mars: frequency, distribution, and implications for flow properties. *Journal of Geophysical Research – Planets*, **115**, E11001.

MARCHANT, D.R. & HEAD, III, J.W. 2007. Antarctic dry valleys: microclimate zonation, variable geomorphic processes, and implications for assessing climate change on Mars. *Icarus*, **192**, 187–222.

MARTÍN-TORRES, F.J., ZORZANO, M.-P. *ET AL.* 2015. Transient liquid water and water activity at Gale crater on Mars. *Nature Geoscience*, **8**, 357–361.

MASSÉ, M., CONWAY, S.J. *ET AL.* 2016. Transport processes induced by metastable boiling water under Martian surface conditions. *Nature Geoscience*, **9**, 425– 428.

MASTERTON, W.L. & HURLEY, C.N. 2011. *Chemistry: Principles and Reactions*. Thomson Brooks/Cole, Belmont.

MCEWEN, A.S., OJHA, L. *ET AL.* 2011. Seasonal flows on warm Martian slopes. *Science*, **333**, 740–743.

MCEWEN, A.S., DUNDAS, C.M. *ET AL.* 2014. Recurring slope lineae in equatorial regions of Mars. *Nature Geoscience*, **7**, 53–58.

MELLON, M.T. & PHILLIPS, R.J. 2001. Recent gullies on Mars and the source of liquid water. *Journal of Geophysical Research – Planets*, **106**, 23165–23179.

MIYAMOTO, H., DOHM, J.M., BAKER, V.R., BEYER, R.A. & BOURKE, M. 2004. Dynamics of unusual debris flows

on Martian sand dunes. *Geophysical Research Letters*, **31**, L13701.

MÖHLMANN, D. & KERESZTURI, A. 2010. Viscous liquid film flow on dune slopes of Mars. *Icarus*, **207**, 654–658.

MORRIS, E. 1982. Aureole deposits of the Martian volcano Olympus Mons. *Journal of Geophysical Research*, **87**, 1164–1178.

MUSHKIN, A., GILLESPIE, A.R., MONTGOMERY, D.R., SCHREIBER, B.C. & ARVIDSON, R.E. 2010. Spectral constraints on the composition of low-albedo slope streaks in the Olympus Mons Aureole. *Geophysical Research Letters*, **37**, L22201.

MUSSELWHITE, D.S., SWINDLE, T.D. & LUNINE, J.I. 2001. Liquid CO_2 breakout and the formation of recent small gullies on Mars. *Geophysical Research Letters*, **28**, 1283–1285.

NUDING, D.L., DAVIS, R.D., GOUGH, R.V. & TOLBERT, M.A. 2015. The aqueous stability of a Mars salt analog: instant Mars. *Journal of Geophysical Research – Planets*, **120**, 588–598.

OJHA, L., MCEWEN, A.S. *ET AL.* 2014. HiRISE observations of Recurring Slope Lineae (RSL) during southern summer on Mars. *Icarus*, **231**, 365–376.

OJHA, L., WILHELM, M.B. *ET AL.* 2015. Spectral evidence for hydrated salts in recurring slope lineae on Mars. *Nature Geoscience*, **8**, 829–833.

PARSONS, D.R. & NIMMO, F. 2010. Numerical modeling of Martian gully sediment transport: testing the fluvial hypothesis. *Journal of Geophysical Research – Planets*, **115**, E06001.

PASQUON, K., GARGANI, J., MASSÉ, M. & CONWAY, S.J. 2016. Present-day formation and seasonal evolution of linear dune gullies on Mars. *Icarus*, **274**, 195–210.

PASQUON, K., GARGANI, J. *ET AL.* In review. Are the different gully morphologies due to different formation processes on the Kaiser dune field? *In*: CONWAY, S.J., CARRIVICK, J.L., CARLING, P.A., DE HAAS, T. & HARRISON, T.N. (eds) *Martian Gullies and their Earth Analogues*. Geological Society, London, Special Publications, **467**.

PELLETIER, J.D., KOLB, K.J., MCEWEN, A.S. & KIRK, R.L. 2008. Recent bright gully deposits on Mars: wet or dry flow? *Geology*, **36**, 211–214.

PHILLIPS, R.J., DAVIS, B.J. *ET AL.* 2011. Massive CO_2 ice deposits sequestered in the south polar layered deposits of Mars. *Science*, **332**, 838–841.

PILORGET, C. & FORGET, F. 2015. Formation of gullies on Mars by debris flows triggered by CO_2 sublimation. *Nature Geoscience*, **9**, 65–69.

PIQUEUX, S., KLEINBÖHL, A. *ET AL.* 2016. Discovery of a widespread low-latitude diurnal CO_2 frost cycle on Mars. *Journal of Geophysical Research – Planets*, **121**, 1174–1189.

POULIQUEN, O. 1999. Scaling laws in granular flows down rough inclined planes. *Physics of Fluids*, **11**, 542–548.

RAACK, J., REISS, D. & HIESINGER, H. 2012. Gullies and their relationships to the dust-ice mantle in the northwestern Argyre Basin, Mars. *Icarus*, **219**, 129–141.

RAACK, J., REISS, D., APPÉRÉ, T., VINCENDON, M., RUESCH, O. & HIESINGER, H. 2015. Present-day seasonal gully activity in a south polar pit (Sisyphi Cavi) on Mars. *Icarus*, **251**, 226–243.

RAACK, J., CONWAY, S.J., HERNY, C., BALME, M.R., CARPY, S. & PATEL, M.R. 2017. Water induced sediment

levitation enhances down-slope transport on Mars. *Nature Communications*, **8**, 1–10.

REISS, D. & JAUMANN, R. 2003. Recent debris flows on Mars: seasonal observations of the Russell Crater dune field. *Geophysical Research Letters*, **30**, 3–6.

REISS, D., VAN GASSELT, S., NEUKUM, G. & JAUMANN, R. 2004. Absolute dune ages and implications for the time of formation of gullies in Nirgal Vallis, Mars. *Journal of Geophysical Research – Planets*, **109**, E06007.

REISS, D., ERKELING, G., BAUCH, K.E. & HIESINGER, H. 2010. Evidence for present day gully activity on the Russell crater dune field, Mars. *Geophysical Research Letters*, **37**, L06203.

RICHARDSON, M.I. & WILSON, R.J. 2002. Investigation of the nature and stability of the Martian seasonal water cycle with a general circulation model. *Journal of Geophysical Research – Planets*, **107**, 5031.

RICHARDSON, M.I. & MISCHNA, M.A. 2005. Long-term evolution of transient liquid water on Mars. *Journal of Geophysical Research – Planets*, **110**, E03003.

SCHON, S.C., HEAD, J.W. & FASSETT, C.I. 2009. Unique chronostratigraphic marker in depositional fan stratigraphy on Mars: evidence for ca. 1.25 Ma gully activity and surficial meltwater origin. Geology, **37**, 207–210.

SCHORGHOFER, N., AHARONSON, O., GERSTELL, M.F. & TATSUMI, L. 2007. Three decades of slope streaks activity on Mars. *Icarus*, **191**, 132–140.

SEARS, D.W.G. & CHITTENDEN, J.D. 2005. On laboratory simulation and the temperature dependence of the evaporation rate of brine on Mars. *Geophysical Research Letters*, **32**, L23203.

SEARS, D.W.G. & MOORE, S.R. 2005. On laboratory simulation and the evaporation rate of water on Mars. *Geophysical Research Letters*, **32**, L16202.

SHINBROT, T., DUONG, N.-H., KWAN, L. & ALVAREZ, M.M. 2004. Dry granular flows can generate surface features resembling those seen in Martian gullies. *Proceedings of the National Academy of Sciences of the United States of America*, **101**, 8542–8546.

SMITH, D.E., ZUBER, M.T. *ET AL.* 2001. Mars Orbiter Laser Altimeter: experiment summary after the first year of global mapping of Mars. *Journal of Geophysical Research – Planets*, **106**, 23689–23722.

SQUYRES, S.W., GROTZINGER, J.P. *ET AL.* 2004. In situ evidence for an ancient aqueous environment at Meridiani Planum, Mars. *Science*, **306**, 1709–1714.

STEWART, S.T. & NIMMO, F. 2002. Surface runoff features on Mars: testing the carbon dioxide formation hypothesis. *Journal of Geophysical Research – Planets*, **107**, 5069.

STILLMAN, D.E., MICHAELS, T.I., GRIMM, R.E. & HARRISON, K.P. 2014. New observations of Martian southern mid-latitude recurring slope lineae (RSL) imply formation by freshwater subsurface flows. *Icarus*, **233**, 328–341.

STILLMAN, D.E., MICHAELS, T.I., GRIMM, R.E. & HANLEY, J. 2016. Observations and modeling of northern mid-latitude recurring slope lineae (RSL) suggest recharge by a present-day Martian briny aquifer. *Icarus*, **265**, 125–138.

STILLMAN, D.E., MICHAELS, T.I. & GRIMM, R.E. 2017. Characteristics of the numerous and widespread recurring slope lineae (RSL) in Valles Marineris, Mars. *Icarus*, **285**, 195–210.

SULLIVAN, R., THOMAS, P., VEVERKA, J., MALIN, M.C. & EDGETT, K.S. 2001. Mass movement slope streaks imaged by the Mars Orbiter Camera. *Journal of Geophysical Research*, **106**, 23607–23633.

TREIMAN, A.H. 2003. Geologic settings of Martian gullies: implications for their origins. *Journal of Geophysical Research – Planets*, **108**, 8031.

TURCOTTE, D.L. & SCHUBERT, G. 2002. *Geodynamics*. Cambridge University Press, Cambridge.

VÉDIE, E.V., COSTARD, F., FONT, M. & LAGARDE, J.-L. 2008. Laboratory simulations of Martian gullies on sand dunes. *Geophysical Research Letters*, **35**, L21501.

WAGNER, W., RIETHMANN, T., FEISTEL, R. & HARVEY, A.H. 2011. New equations for the sublimation pressure and melting pressure of H_2O ice Ih. *Journal of Physical and Chemical Reference Data*, **40**, 043103.

WESTOBY, M.J., BRASINGTON, J., GLASSER, N.F., HAMBREY, M.J. & REYNOLDS, J.M. 2012. 'Structure-from-Motion' photogrammetry: a low-cost, effective tool for geoscience applications. *Geomorphology*, **179**, 300–314.

WILLIAMS, K.E., TOON, O.B., HELDMANN, J.L. & MELLON, M.T. 2009. Ancient melting of mid-latitude snowpacks on Mars as a water source for gullies. *Icarus*, **200**, 418–425.

YAWS, C.L. 2015. *The Yaws Handbook of Vapor Pressure: Antoine Coefficients*. Gulf Professional Publishing, Oxford.